Urban Infrastructure Damage Detection and Mapping Using Sentinel 1

Padmini Manivannan

Technische Universiteit Delft

TU Delft

Urban Infrastructure Damage Detection and Mapping Using Sentinel 1

by

Padmini Manivannan

to obtain the degree of Master of Science
at the Delft University of Technology,
to be defended publicly on Monday August 26, 2019 at 09:00 AM.

Student number:	4714474	
Project duration:	January 1, 2019 – August 26, 2019	
Thesis committee:	Dr. ir. Paco Lopez Dekker,	TU Delft, supervisor
	Prof. dr. ir. Alle-Jan van der Veen,	TU Delft
	Dr. Ir. Faruk Uysal,	TU Delft

An electronic version of this thesis is available at `http://repository.tudelft.nl/`.

TU Delft

Preface

This master thesis project was an interdisciplinary research project carried out with the Electrical Engineering, and Civil Engineering and Geosciences departments of the Delft University of Technology. This research aims to design an effective methodology to rapidly detect and map infrastructural damage in urban areas after natural or man-made disasters.

As a six-year-old, I was in Gujarat when the Mw 7.7 Bhuj earthquake struck. The events and the aftermath of the earthquake are seared into my memory. At that point, I didn't realise the kind of impact this would have on me. It started as an innocent curiosity to know more. Ideas related to earthquakes and damage detection have always piqued my interest. In the fourth quarter of my Master's, I studied a course called Geodesy and Natural Hazards, taught by Paco Lopez Dekker, who would eventually be my thesis supervisor. Here, I saw the opportunity to use my signal processing background to an application that I found myself very invested in.

This thesis would not have been possible without the incredible guidance and encouragement of my supervisor, Dr. Paco Lopez Dekker, as well as my thesis committee members, Dr. Alle-Jan van der Veen and Dr. Faruk Uysal. A special thank you to Malte Manne for your help and patience.

To Leon, Pooja, Magne, Jens, Ines, Roosa, Nikhil - you created a safe space for me far away from home. Thank you for all your care, love and support. Finally and most importantly, I'd like to thank my family for the love, encouragement and the values you instilled in me.

Padmini Manivannan
Delft, August 2019

The cover image shows the Sentinel 1 satellite, the first of the Copernicus missions. Photo: ESA/ATG medialab. Image downloaded from https://www.esa.int/spaceinimages/Images/2014/02/Sentinel-12

Abstract

Natural or man-made disasters can have a drastic impact on social, economic and environmental aspects of an affected population. Specifically, earthquakes are one of the most potent natural hazards, which cause a disproportionate amount of fatalities, primarily due to a) unexpected building collapses, b) restricted or limited access to basic amenities and c) potential hazards following earthquakes such as landslides, tsunamis etc.

It is crucial to have an overview of the infrastructural damage caused following a disaster for search and rescue services to assess the extent of the damage. For the purpose of this research, Sentinel 1 imagery is used to map the building damage in an urban area after a disaster. A combination of parameters such as persistent scatterers, pixel amplitude and phase is used with a timeseries of full-resolution and spatially averaged radar images. Points that are stable in amplitude over a long timeseries, also known as Persistent Scatterers, are extracted from a stack of full-resolution images. The amplitudes of persistent scatterers, along with amplitude and coherence of pixels derived from a stack of spatially-averaged images, are statistically analysed to check the trends of the parameters pre- and post the disaster. A change detection algorithm is applied to this stack in order to localise the areas of building damage. The results are superimposed on Google Earth for easy interpretation using a graded damage scale.

The analysis shows that exploiting the persistent scatterer amplitudes in the manner used in this research provides a novel way of locating building damage. This technique can be used effectively in urban areas. Using a combination of pixel amplitudes and coherence along with the persistent scatterers helps correctly find new and unique points of damage for each parameter used. The results were validated using reference Grading and crowd-sourced maps. The results illustrate that the proposed approach can be used for detecting and producing informative maps on infrastructural damage detection in urban areas.

Contents

List of Figures

List of Tables

1
Introduction

Natural and man-made hazards, such as earthquakes or warfare, can cause a potential humanitarian crisis. According to the World Health Organisation (WHO), natural disasters kill around 90,000 people and affect around 160 million people worldwide every year [52]. This number is likely to increase with global warming, due to the risks it brings such as extreme weather. These disasters have an immediate impact on human lives and cause destruction of biological, physical and socio-environmental aspects of the affected people. To prevent or minimise the damage to human life, it is necessary to have a method to analyse the situation to enable planning and response.

Among natural disasters, earthquakes are one of the most potent natural hazards, causing massive destruction. Building damage due to such hazards can have a direct or indirect impact on valuable human life and property. The major factors that contribute to human casualty in cases of natural or man-made hazards are unexpected collapsing of structures, getting stuck under rubble without access to food or water and 'follow-on' disasters such as landslides, tsunamis caused directly due to the main disaster. Although a healthy human can survive three to five days under rubble without food or water [29], studies show that structural collapses are the cause for 75% of deaths in earthquakes [10].

Hence, it is important to provide a method to rapidly map and localise the points of building damage as soon as possible after disasters, since it is a crucial period to find any survivors. A lack of a clear overview of the situation caused by inaccessible roadways or damaged communication systems can hinder an efficient search and rescue operation [2]. This indicates a need for preliminary information on damage localisation in the form of damage maps.

1.1. Research Motivation

For any search and rescue team to be efficient in their functionality, it is important to provide a preliminary assessment of the building damage as soon as possible after the disaster. Ground-based gathering of such evidence is cumbersome and time-consuming. The team is also possibly be affected by a lack of mobility due to the disaster. Remote sensing methods prove to be a good alternative to this. It provides a clear overview and an aerial perspective. Although, it poses an additional challenge to produce the damage maps as quickly as possible after the post-disaster image is made available.

There are various options available for remote-sensing data such as LIDAR (LIght Detection And Ranging of Laser Imaging Detection And Ranging), RADAR (RAdio Detection And Ranging), or optical imagery. They are also acquired at varying distances from the surface of the earth in the form of airborne and space-borne satellites. The airborne satellites like drones can be very effective for quick mapping but its availability depends on the country's resources. Space-borne satellites can provide the imagery of a very large area periodically and is generally a more readily available source of data. It is also a reliable source which can provide imagery that is largely unaffected by the weather or time of day.

Synthetic Aperture Radar (SAR) is a promising source of radar data. It is a radar system which generates high-resolution images by using the flight path of the satellite in order to simulate a very large antenna (or aperture). Man-made structures have a consistent electromagnetic backscattering signal and any changes in the structures are likely to cause an inconsistent backscatter compared to the previous pass. This change in backscatter can be picked up as a change in comparison with the previous image.

While SAR radar imagery has been widely used for rapid damage mapping in case of disasters by various organisations such as the Advanced Rapid Imaging and Analysis (ARIA) group of the Jet Propulsion Laboratory (JPL), Copernicus Emergency Management Service (EMS) or the International Charter Space and Disasters, they do not fully utilise the advantages provided by time-series analysis. In order to reliably detect a change in the post-disaster image, it is useful to have a set of pre-disaster images whose amplitude and coherence trends can be studied.

The Sentinel-1 mission launched by the European Space Agency consists of a constellation of two satellites (Sentinel-1A and Sentinel-1B) that operate day and night and produce C-band imagery. The constellation is on a near-polar, sun-synchronous orbit. While it has a medium (5 m by 20 m) spatial resolution, it has a higher temporal resolution than older satellites such as ERS-1/2 and ENVISAT ASAR. It has a repeat cycle of 12 days and at the equator, it has a 6-day repeat cycle due to the two-satellite constellation. Sentinel offers four types of data products and the Level 1 Single Look Complex (SLC) and Ground Range Detected (GRD) products are made available for specific Near Real-Time (NRT) areas within one hour of acquisition and within 24 hours for all other regions. Due to its open-data policy and high temporal resolution, the Sentinel-1 imagery is a promising dataset for rapid disaster response.

1.2. Aim of the research

The aim of this research is:

To design a methodology that combines a timeseries of multiple SAR parameters in order to create damage detection maps in case of a disaster.

This main aim can be divided into research questions as follows:

1. How can the Sentinel 1 archive be used effectively for detecting building damage?
   An integral part of the research is to utilize a time-series of Sentinel-1 imagery and determining if it can be used in an effective manner to localise building damaged due to natural disasters. The algorithm will use information gathered from the pre-disaster time-series to locate changes in the post-disaster image.

2. How can the use of amplitude and coherence parameters be combined to produce the damage maps?
   According to the literature survey, amplitude and coherence are useful in picking up different intensities of damage. Hence, it is useful to combine the use of these parameters to produce the final maps for relief response.

3. Can full resolution Sentinel 1 images be utilised effectively along with spatially averaged (or multi-looked) images?
   The full resolution radar images contain pixels, which in case of Sentinel-1, has a resolution of 5 m by 20 m. Points that are stable natural reflectors are called Persistent or Permanent Scatterers [18] are selected from the full resolution image, upon which the change detection method is applied. These points are thoroughly discussed in Section 3.2.1. Additionally, spatially averaging the images would cause a blurring of the edges (detrimental to selecting persistent scatterers) but the function also reduces speckle noise. Hence, after spatially averaging, we consider the amplitude and coherence values as input for the change detection algorithm again. It helps detect damaged areas which are missed by using persistent scatterers. In case similar results are derived from all three parameters, it also helps to reinforce and validate the results.

4. Are the resulting damage maps sufficiently informative?
   It is important that the results of the algorithm produce maps that are easy to understand and provide preliminary information that describes where the damages are localised.

2

Background Information

When hazards strike in highly vulnerable areas with a high population and inappropriately managed risk, it is called a disaster [28]. This could be a natural disaster such as cyclones, floods, earthquakes, tornadoes etc. or a man-made disaster such as wars, oil spills, nuclear explosions, fires etc. Both can cause large scale destruction of valuable human life and property and leave significant economic damage in its wake.

Earthquakes can be particularly destructive since it usually occurs without warning or with little warning. Between 1998 and 2017, 7.8% of all natural disasters were earthquakes but this resulted in a disproportionate percentage of deaths, which is 56%, over the same time period [51]. Figure 2.1a shows the number of recorded earthquakes between 1990 and 2018 while Figure 2.1b shows the disproportionate number of fatalities due to those earthquakes in the same time period.

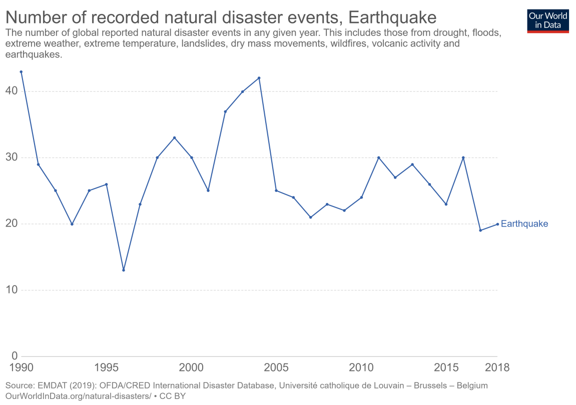

(a) Number of recorded earthquakes between 1990 and 2018 [14]

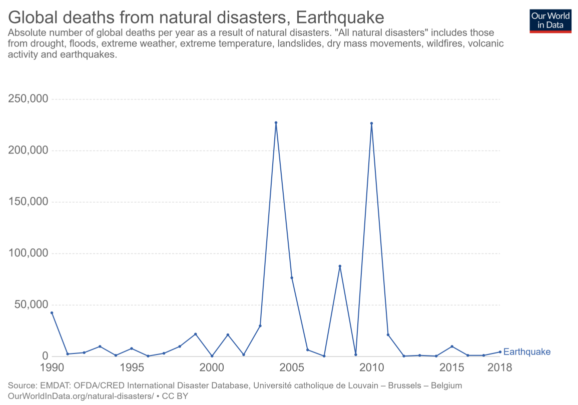

(b) Global deaths recorded due to earthquakes between 1990 and 2018 [14]

Figure 2.1: The Figure on the left shows the number of recorded earthquakes between 1990 and 2018 and the Figure to the right shows the global fatalities between 1990 and 2018 due to earthquakes. Earthquakes are responsible for a disproportionate number of fatalities when compared to the number of earthquakes that occur over the same time period.

There are various methods in which disasters can be monitored and surveyed. Before remote sensing technology came to be used commonly, ground-based surveying was done using rescue teams. Since manually gathering information is cumbersome and time-consuming, remote sensing methods are preferred. Some of the technologies used for this are airborne and spaceborne platforms with sensors like optical and infrared systems. Optical sensors can provide high-quality images are have been used widely for damage detection purposes. It depicts the surfaces it images as seen by the human eye, hence making it easy to interpret. However, they require smoke and smog-free conditions and are limited to usage during the availability of daylight. Unmanned Air Vehicles (UAVs) can be a good source of imagery for monitoring since they can capture high-resolution data and transmit to the ground station in NRT but its usage usually depends on the resources of the affected area.

LIDAR, also known as Airborne Laser Scanning (ALS) uses a laser to measure the distance between the sensor and the point that is sensed. ALS technology usually delivers point clouds and integrates an airborne laser, a global positioning system (GPS) and inertial measurement technology. It has been used successfully in the context of emergency relief and management [36, 49, 50]. In LIDAR, short wavelengths of the electromagnetic spectrum are used and hence it is highly sensitive to clouds, rain or smog.

Synthetic Aperture Radar (SAR) systems can record both the amplitude and phase characteristics of the backscatter signal. One of the biggest advantages is that it can be used irrespective of sunlight and weather conditions. It has been widely used to assess damages after disasters [33, 38]. By analysing the amplitude or coherence values one can discriminate between damaged or undamaged structures. While SAR images have been used widely by various organisations such as Copernicus Emergency Management Services (EMS) or Global Disaster Alert and Coordination System, they do not fully utilise the potential of the Sentinel constellation by not using a long time-series of data.

Since its launch, the Sentinel 1 satellite has provided a steady stream of radar images with a repeat cycle of 6-12 days depending on the area under consideration. It has a C band synthetic aperture radar (SAR). Processed Level 1 Single Look Complex (SLC) data is considered for the analysis in this research since it is a complex image with amplitude and phase information. The various SAR parameters under consideration for this research are intensity, phase and a combination of intensity and phase.

While most approaches commonly use the amplitude and coherence for change detection purposes in case of disasters, Persistent Scatterer Interferometry (PSI) has been mostly restricted to improving Digital Elevation Models (DEMs) and studying minute or slow variation (1mm/year) in the topography. Persistent Scatterers are points that are found to be stable in amplitude over a long period of time. These points usually represent man-made reflectors like roads, the side, or the tops of buildings or structures. The outputs of the PSI approach are the velocity and height of the changed point. The PSI method is discussed, by reviewing the seminal paper published by Ferretti et al. [18], and some other papers using similar techniques to provide an overview of the way persistent scatterer points are generally used. Before we dive into what the literature says, some SAR basics are elucidated.

2.1. Synthetic Aperture Radar

In radar, a high power pulse is transmitted that can be visualised as a modulated waveform embedded in a carrier [23]. This can be described by the equation:

$$s_T(t) = a_T u(t) + \cos(wt + \phi(t)), \tag{2.1}$$

where a_T is the constant transmitted amplitude, $u(t)$ is the pulse envelope, w is the carrier frequency and ϕ is the phase modulation. Assuming a stationary target at a certain range r, the received signal consists of reflection from the object along with some noise. The delay time in receiving the reflected pulse is given by $\tau = 2r/c$, where c is the speed of light. Hence, the received signal can be described by the equation:

$$s_R(t) = a_R u(t-\tau)\cos(w(t-\tau) + \phi(t-\tau) + \phi_o) + n(t), \tag{2.2}$$

where a_R is the received amplitude signal, ϕ_o is the unknown phase shift of the received signal, n is the noise signal and the received signal has a delay of τ. In order to process in phase and quadrature phase signals, we multiply the received signal by sin and cos and low pass filter it [23]. Then the two (in phase and quadrature) signals can be given by,

$$z_I(t) = a_R(t)u(t-\tau)\cos(\phi_o - w\tau + \phi(t-\tau)) + n_I(t) \tag{2.3}$$

$$z_Q(t) = a_R(t)u(t-\tau)\sin(\phi_o - w\tau + \phi(t-\tau)) + n_Q(t) \tag{2.4}$$

which can be simplified and now the complex signal is,

$$\begin{aligned} \underline{z}(t) &= a_R u(t-\tau)\exp(j(\phi_o - w\tau))\exp(j(t-\tau)) + \underline{n}(t), & (2.5)\\ &= \underline{a}u(t-\tau)\exp(j\phi(t-\tau)) + \underline{n}(t), & (2.6)\\ & & (2.7) \end{aligned}$$

with $\underline{\mathrm{a}} = a_R \exp(j(\phi - w\tau))$, being the complex amplitude and $\underline{\mathrm{n}}$ is the complex noise.

This is the signal that is received by the receiver in the satellite. The imagery used in this research is acquired from the Sentinel 1 satellite in Terrain Observation with Progressive Scans SAR (TOPSAR) imaging technique or mode. This is similar to the ScanSAR mode since the images are acquired in bursts. The images are acquired in bursts and in each burst, the radar beam is electronically moved from one side to another in the azimuth direction [15] as shown in Figure 2.2b. This is done over several 'sub-swaths' in range. In Figure 2.2a, the general terms associated with SAR are shown in a schematic diagram [5]. The strips acquired side by side are in the azimuth direction and in this case, is the direction of flight of the satellite. The range direction is perpendicular to the azimuth.

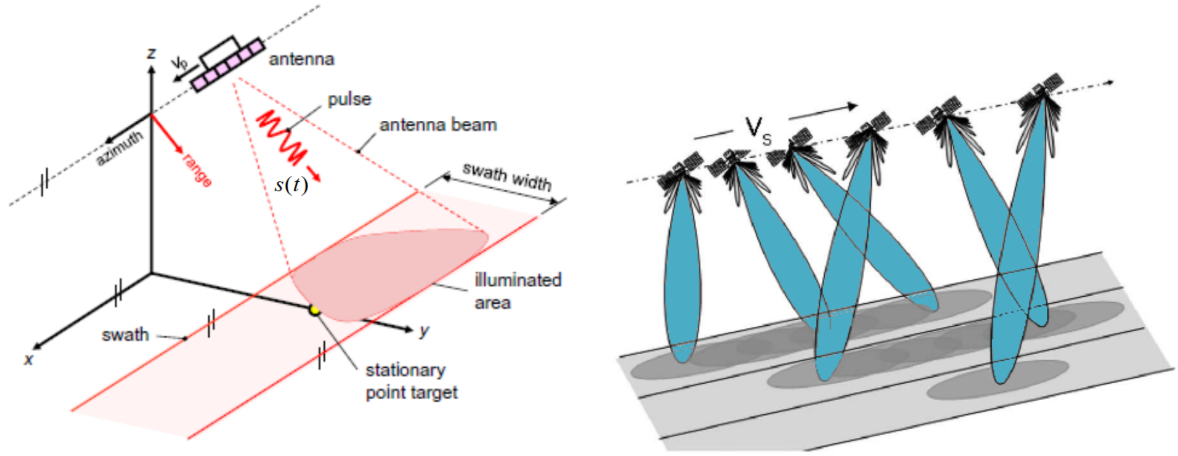

(a) Figure illustrating SAR acquisition geometry; from [5]

(b) Figure illustrating Sentinel 1 TOPSAR mode. The images are acquired over several bursts in azimuth and over multiple sub-swaths in range; from [15]

Figure 2.2: Figures showing SAR geometry to the left and the TOPSAR mode used in Sentinel 1, a type of ScanSAR mode

The input files that are used for the research come in the form of SLC images. A complex (I and Q) value represents each pixel in the SLC and hence contains both amplitude as well as phase information [16]. The amplitude signal refers to the strength of the radar response or backscatter and intensity refer to the square of the amplitude. The phase depends primarily on the distance between the target and sensor. The relationship is given by [8]:

$$\phi = -\frac{4\pi}{\lambda}R + \phi_{error}, \tag{2.8}$$

where λ is the wavelength of the radar signal, R is the sensor-target distance and ϕ_{error} is the phase error due to delay in the signal. Interferometric SAR uses the phase difference between two complex images of the same area, acquired from slightly different geometries to extract the distance information.

SAR can be used to locate damaged buildings by using the amplitude and/or the phase pixels in the images. In the following section, a review of relevant background information is provided. The SAR parameters used for change detection are discussed along with the PSI algorithm.

2.2. Intensity

The use of intensity for damage detection has produced some consistent results. **Matsuoka and Yamazaki** [34] use ERS satellite images to study the damage occurred during the 1995 Kobe earthquake. It was argued that although the phase approach has a higher degree of sensitivity, using intensity has a requires a low dependence on the conditions mentioned above and hence may be developed as a uniform method to detect damaged areas.

The effects of pixel window size and speckle noise is also analysed while evaluating damage.The use of the backscattering coefficient and correlation coefficient of the (four) pre-disaster and (five) post-disaster scenes were investigated. The first parameter used for damage detection is the correlation coefficient, r, between two intensity images a and b which is calculated as

$$r = \frac{N\sum_{i=1}^{N} Ia_i Ib_i - \sum_{i=1}^{N} Ia_i \sum_{i=1}^{N} Ib_i}{\sqrt{(N\sum_{i=1}^{N} Ia^2{}_i - (\sum_{i=1}^{N} Ia_i{}^2)) \cdot (N\sum_{i=1}^{N} Ib^2{}_i - (\sum_{i=1}^{N} Ib_i{}^2))}}, \tag{2.9}$$

where i is the pixel number, Ia_i and Ib_i are the backscatter values of the two images averaged over a window containing N pixels. The second parameter used is the backscattering coefficient, d, as shown in the equation

2.10

$$d = 10 \cdot log_{10} \bar{I}a_i - 10 \cdot log_{10} \bar{I}b_i, \tag{2.10}$$

where $\bar{I}a_i$ and $\bar{I}b_i$ are the averaged intensity values over the pixels surrounding pixel number, i, within a 13 × 13 window. From the two parameters, a regression determinant score given by a discriminating line that differentiates between an area that has a damage ratio of 100% and an area with no damage using two indices, r and d. Here, damage ratio refers to ratio of number of building classified as damaged and the total number of buildings in the block. The discriminating line equation is given by,

$$\alpha d + \beta r + \gamma = 0, \tag{2.11}$$

and a discriminant score, z, is calculated where,

$$z = \alpha d + \beta r + \gamma, \tag{2.12}$$

which provides a distinction between severely damaged and non damaged areas depending on whether is it positive or negative. A relative good agreement was found between the results of the research and a field survey by the Architectural Institute of Japan and the City Planning Institute of Japan. The disadvantage of this method is that the discriminant score changes based on the area and its urban structure under consideration.

2.3. Phase

Matsuoka and Yamazaki [32] use coherence analysis of SAR data for earthquake damage detection during the 1995 Kobe earthquake. 5 pre-disaster and one post disaster JERS-1 images are used to calculate the coherence, which describes the degree of correlation between the images. It is a sensitive parameter for change detection. The images were co-registered to form two pre-seismic (two images before the seismic event, which refers to the earthquake) and two co-seismic (images immediately preceding and following the seismic event) image pairs followed by calculation of the coherence. The complex coherence γ of complex signals a_1 and a_2 is defined in the equation 2.13

$$\gamma = \frac{\sum_{i=1}^{N} a_{1i} a_{2i}^*}{\sqrt{\sum_{i=1}^{N} |a_{1i}|^2} \sqrt{\sum_{i=1}^{N} |a_{2i}|^2}}, \tag{2.13}$$

where N is the number of signal measurements (pixels) and i is the sample number. Matsuoka and Yamazaki [32] conclude that an increase in building damage caused a decrease in the magnitude of the coherence.

Fielding et al. [20] investigate the use of interferometric correlation measurements from Envisat images to map the details of the damage caused due to the 2003 Bam, Iran earthquake. The complex correlation is calculated for the single pre-seismic pair and two the co-seismic pairs as shown in (2.13). They note that spatial averaging while correlation estimation can be underestimated due to a phase gradient through the averaging window [7]. This phase gradient may be are due to interferometric baselines and topography (which can be removed before calculations) and co-seismic deformation of the surface (which is more difficult to remove). To avoid this, the window sizes can be reduced but it leads to an overestimation of the coherence [25]. An alternative suggested was to use the phase variance σ_ϕ^2 to calculate the coherence. This is done using the phase-sigma correlation [42]. This is done by first removing any local ramp or phase trend (de-ramping) followed by calculating the variance of the phase in that region using

$$\sigma_\phi = \frac{1}{\sqrt{2N}} \sqrt{\frac{1-\gamma^2}{\gamma^2}}, \tag{2.14}$$

where N is the number of samples and γ can be isolated to get,

$$|\gamma| = \frac{1}{2N{\sigma_\phi}^2 + 1}. \tag{2.15}$$

A 5×5 window was used to calculate the coherence using equation 2.14. In order to differentiate between correlation change between vegetated areas and correlation change due to structural damage of buildings, a correlation difference map was generated by subtracting the pre-seismic correlation map from the co-seismic image pair. Hence, negative correlation values indicate damage caused due to the earthquake. A 100% destruction of buildings in the old parts of the city resulted in a correlation change from -0.7 to -0.3 on the correlation change map. It is to be noted that the correlation difference method works best with low baselines

Table 2.1: Damage class categories for coherence change index, ρ, as defined by Hoffmann [26]. This is used to threshold the levels of coherence change index to correspond to varying levels of damage.

Average coherence index	Damage level class
$\rho < 1.5$	No damage
$1.5 \leq \rho < 2.0$	Light damage
$2.5 \leq \rho < 2.5$	Significant damage
$\rho \geq 2.5$	Severe damage

and a low random noise component since the SNR decreases if the subtracted images have a high random noise component.

Hoffmann [26] utilises a coherence change index which can be quantitatively interpreted in terms of the extent of damage during a catastrophic event. This particular study focuses on the Bam earthquake of 2003. They also show that the results are robust when image pairs with varying temporal and perpendicular baselines are used. One pre-disaster and three co-disaster (images immediately preceding and following a disaster) image pairs were created and a 4 × 20 window is used to calculate the coherence using (2.13). The mean coherence level generally decreases for all co-seismic interferograms compared to the pre-seismic ones. To quantify this change, a coherence change index ρ is computed which is given by

$$\rho = \frac{\gamma_{ref}}{\gamma_{eq}}, \tag{2.16}$$

where γ_{ref} is the coherence computed for the interferogram before the earthquake and γ_{eq} refers to the same spanning the earthquake. A common bandwidth filter is also used to reduced the effects induced due to long baselines (spatial correlation) at the cost of reduced range resolution [22]. The average coherence index is computed as

$$\bar{\rho} = \frac{1}{N} \sum_{i=1}^{N} min(\rho_i, 3), \tag{2.17}$$

where N is the number of image pixels, All the values are thresholded below 3. Damage categories were assigned for different ranges of the average coherence index as shown in Table 2.3 Close agreement was found between the regions of highest damage in the coherence index images and severe damage visible from the IKONOS optical images for all the co-disaster pairs. It is to be noted that common bandwidth filtering is best used on a relatively flat terrain such as Bam. To avoid incorrect estimation of damage, it is better to consider a pre-disaster image pair with a short baseline and use it with a co-disaster image pair with a similar baseline.

Yun et al. [53] use the Italian Space Agency's COSMO-SkyMed (CSK) SAR (X-band) and the Japan Aerospace Exploration Agency's ALOS-2 (L-band) satellite to acquire images over the Gorkha are in Nepal during the 2015 earthquake. With three images from each satellite, two image pairs were formed, one pre-seismic and one co-seismic. The coherence maps were produced and estimated over a 3 × 3-pixel window size using (2.13) after topographic phase removal using the 1-arcsec Shuttle Radar Topography Mission (SRTM) digital elevation model (DEM). The pixel values were adjusted to removed pixel bias [24]. The coherence maps were registered to each other after calculating dense sub-pixel offsets following which the resampled maps were 'matched' using histogram matching such that the statistics are identical to the reference (pre-seismic) coherence maps. They then take the difference of the coherence maps and apply a colour map to produce the Damage Proxy Map (DPM). Validation showed that the maps showed good correlations between the CSK DPM and the National Geospatial Agency's analysis and the United Nations Operational Satellite Applications Programme's damage assessment maps.

2.4. Phase and Intensity

The general idea used here is that the interferometric coherence in general reduces, and there is a decorrelation of data between two images before and after a natural disaster. This is used in combination with intensity changes, on the basis of different backscattering behaviour due to geometric changes in the structures scattering the waves.

Matsuoka and Yamazaki [33] proposed to use multiple parameters to study the 1999 Kocaeli, Turkey earthquake using ERS-1 and ERS-2 data. They use three pre-disaster and one post-disaster acquisition. All

Table 2.2: Feature sets in terms of n-dimensional vectors as defined by Stramondo et al. [44]. Different feature vector types and sizes are used to classify regions into different levels of damage.

Type	Vector size	Components
COHER	3D vector	pre-, post- and co-seismic coherence
CORREL	3D vector	pre-, post and co-seismic correlation
SAR	8D vector	vector COHER, vector CORREL, pre- and post-seismic SAR intensity image
OPT	2D vector	pre- and post seismic IRS image
OPT + SAR	10D vector	vector SAR and vector OPT
OPT + COHER	5D vector	vector COHER and vector OPT

the images were registered to the master image using the nearest neighbour method at the position with the highest correlation between two single look amplitude image. The master image refers to the reference image on top of which other 'slave' images are overlapped or 'co-registered' upon. The parameters used for change detection are coherence (2.13), amplitude correlation (2.9) and amplitude difference (2.10).

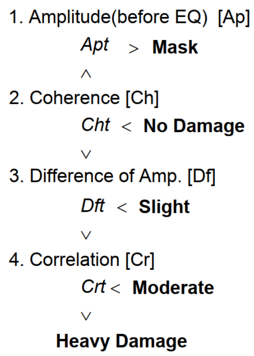

Figure 2.3: Procedure for Damage Detection as used by Matsuoka and Yamazki [33]. A layered approach is taken wherein different parameters like coherence, amplitude difference and intensity correlation are used to ascertain the level of damage.

Matsuoka and Yamazaki [33] use a layered approach and assign thresholds for each parameter. It was found that intensity difference can describe large surface changes, intensity correlation can detect a wide array of earth surface changes and coherence is sensitive to small surface changes. Therefore, they use coherence to differentiate damaged areas from non-damaged areas, amplitude difference to detect slight damage and correlation to detect moderate or heavy damage depending on whether it is above or below the threshold. The results show relatively good agreement with various damage survey reports.

Stramondo et al. [44] explores the use of SAR data along with optical satellite data in the areas of Bam, Iran (2003 earthquake) and Izmit, Turkey (1999 earthquake). SAR images are first coregistered, followed by image intensity I calculation. To reduce speckle noise, the images are multi-looked using the Goldstein filter [31]. The complex coherence is calculated as in 2.13 and the intensity correlation is calculated using 2.9. The classification of regions into different levels of damage is done using different combinations of n-dimensional feature vectors. The vectors are used to understand which parameters contribute to discriminate change. They conclude that using OPT vector along with the COHER vector give the highest overall accuracy, that is, using the complex coherence combined with optical images results in higher classification accuracy.

Arciniegas et al. [3] studied the area of Bam, Iran during the 2003 earthquake using ENVISAT radar images. The complex coherence is calculated using (2.13) over a 25×5 moving window. Change in amplitude is also used as a factor to evaluate the damage. They conclude that earthquake damage caused both an increase and decrease in amplitude, therefore only the absolute value was taken into consideration and that using both parameters lead to higher accuracy than using them individually. They note that using coherence individually produced better results than using absolute amplitude changes, although with limited accuracy.

Gamba et al. [21] use a combination of intensity and phase features for damage classification. Ancillary data in the form of GIS layers are also used to improve the accuracy of the maps. The change detection algorithm itself is based on a neural-network classifier or a Markovian Random Field (MRF). They also note that the best results were obtained by using the intensity values alone, contrary to Arciniegas et al. [3].

Trianni and Gamba [45] exploit multi-temporal SAR data and ancillary information for defining urban damage. These approaches are applied to the areas of Bam (Iran), Boumerdes (Algeria) and Pisco (Peru). Two approaches are proposed, one, a fast and low precision analysis, an unsupervised statistical analysis of variables that represent backscatter intensity or coherence values for the area under analysis. The second approach is a supervised method involving a multi-temporal classifier, performed using a Markov Random Field (MRF) or a neural network classifier.

In the unsupervised approach, statistically significant parameters are extracted from the SAR images. The urban area is divided into blocks level and a statistical analysis characterises these blocks. A lognormal or Weibull distribution is used for the characterisation was proved to be reliable by Stramondo et al. [43]. In the analysis of radar images, a Weibull distribution is preferred when the main parameter in consideration is backscatter intensity while a lognormal distribution is preferred over urban areas since it adapts better to abrupt changes in intensity due to strong backscatter commonplace in urban areas.

From the statistical analysis of block-level histograms of the damaged areas, they observe a reduction of mean amplitude and decrease in the variance values. They conclude that the variance V is an important parameter for change detection. Suitable thresholds are set - in this case, a variance change of more than 10% is assumed to be an indicator of damage. This approach, however, is imprecise especially when the damage level is relatively low.

2.5. Persistent Scatterer Interferometry

Ferretti et al. [18] present a process of the identification and exploitation of stable, natural reflectors, also known as Persistent Scatterers (PSs). Using this approach, a millimetre level motion detection can be achieved. PSs are coherent over long time intervals and can be utilised very effectively for multi-temporal analysis. The final product of such an analysis would be elevation and line of sight velocity of the PSs in the form of a deformation map. In order to achieve millimetre level of precision, atmospheric artefacts that create an Atmospheric Phase Screen (APS) are estimated and removed.

Let Φ indicate a [K × H] matrix of interferometric phases of H pixels considered as PS candidates and K+1 is the number of SAR images. Then, Φ is given by,

$$\underline{\Phi} = \underline{a}\underline{1}^T + \underline{p_\xi}\underline{\xi}^T + \underline{p_\eta}\underline{\eta}^T + \underline{B}\underline{q}^T + \underline{T}\underline{v}^T + \underline{E}, \tag{2.18}$$

where $\underline{a}$ [K × 1] has constant phase values, $\underline{p_\xi}$ [K × 1] and $\underline{p_\eta}$ [K × 1] are the slopes of phase components along azimuth ($\underline{\xi}$) [H × 1] and slant range ($\underline{\eta}$) [H × 1] because of atmospheric phase contributions. $\underline{B}$ [K × 1] has perpendicular baseline values, $\underline{q}$ [H × 1] contains the elevation of each PS multiplied by $4\pi/(\lambda R\sin\alpha)$. Here, R is the radar sensor to target distance, α is the local incidence angle with respect to the reference ellipsoid (geodetic system) and λ is the SAR wavelength. $\underline{T}$ [K × 1] has the time interval between K slave images and the master. $\underline{v}$ [H × 1] has the slant range velocities of the PS's and $\underline{E}$ [K × H] has the residual atmospheric effects, phase noise etc. This is a non-linear system of equations since the phase values are wrapped modulo 2π. Thus, Φ describes a wrapped observation. It is to be solved by an iterative algorithm initialised using an available DEM. The estimated geometric phase component is subtracted from the interferometric phase Φ to get zero baseline steered interferometric phases,

$$\underline{\Delta\Phi} = \underline{a}\underline{1}^T + \underline{p_\xi}\underline{\xi}^T + \underline{p_\eta}\underline{\eta}^T + \underline{B}\underline{\Delta q}^T + \underline{T}\underline{v}^T + \underline{E}, \tag{2.19}$$

where $\underline{p_\xi}$ and $\underline{p_\eta}$ take into account APS and orbital indeterminations. With Sentinel 1, this is not required because the orbits are very controlled and follow nearly the same orbit each pass. The system 2.19 can be solved and the unknowns $\underline{a}, \underline{p_\eta}, \underline{p_\xi}, \underline{\Delta 1}$and $\underline{v^T}$ can be estimated if the SNR is high enough, a constant velocity model is applicable to the targets and the APS can be approximated as a phase ramp.

To identify PSs, coherence maps associated with the interferograms are exploited. The amplitude values of each pixel of the time series are analysed. The phase dispersion is estimated fromthe amplitude dispersion because the amplitude is unaffected by certain factors such as APS, orbital in-determinations, terrain deformation or DEM errors. The phase dispersion, σ_v is estimated from the amplitude dispersion (D_A),

$$\sigma_v \approxeq \frac{\sigma_A}{m_A} \triangleq D_A, \tag{2.20}$$

where m_A and σ_A are the mean and standard deviation of the amplitude values. The dispersion index D_A is a measure of phase stability. Small values of D_A are found to be good estimates of phase dispersion. After the

PSCs are selected, 2.19 is solved using an iterative algorithm. Following this, APS is estimated and removed, DEM errors Δq and target velocity $\underline{v}$ are estimated pixel by pixel by maximising the phase coherence of each pixel. While this has a high level of accuracy, in the order of millimetres, not all buildings can be monitored this way. This approach was applied to the area of Merche in Central Italy, an area known for its instability. Comparing the velocity fields with the ground truth data confirms the reliability of the results. This method has also been applied by Bakon et al. [4] to the area of Bratislava, Slovakia with successful results.

Several other methods have been proposed based on PSs post this paper. **Berardino et al.** [6] suggested using data pairs with small orbital separation in order to lower the spatial decorrelation phenomena. Then, Singular Value Decomposition (SVD) is applied in order to "connect" SAR acquisitions with a large baseline so as to increase the observation temporal sampling rate. Atmospheric Phase artefacts are identified and filtered out due to the availability of spatial and temporal information.

Since most of the previous methods related to PSs were vastly effective only in urban areas, **Ferretti et al.** [19] proposed SqueeSAR, which overcomes the limitations of PSInSAR. They provide an algorithm to jointly process PSs and Distributed Scatterers (DSs). DSs refer to areas of moderate coherence in some interferometric pairs. These pixels usually correspond to a single large object such as desert areas, debris areas etc.

They spatially average the data of statistically homogeneous regions or pixels (SHP) using the Kolmogorov-Smirnov test. This is known as DespecKS algorithm. After this, a coherence matrix is estimated after which a phase triangulation algorithm (PTA) is applied to these coherence matrices corresponding to each DS. The DSs are finalised using a threshold according to the values of γ_{PTA} which is similar to the ensemble coherence for PSs. Then the original SAR phase values are replaced with the optimised phase values. after which point regular PSInSAR processing is carried out as explained in Ferretti et al. [18].

Review The studies discussed above show the different ways in which damage due to disasters can be detected using SAR technology. Table 2.5 shows a summary of these methods for a simpler overview. We find that building damage can be detected by using amplitude, coherence or a combination of both. This is because amplitude and coherence are sensitive to different backscattering behaviour. We have also seen that coherence is a better parameter to detect small variations and amplitude is very useful in detecting large scale changes. Hence, there is great value in using a combination of both, by making use of complex SLC images.

Most of these images require some form of averaging or filtering which comes at the cost of spatial resolution. This affects the possibility of detecting individual building damage. It would be useful to use full resolution images in addition to using spatially averaged images for amplitude and coherence analysis. Additionally, the concept of adaptive spatial averaging (also refered to as adaptive multiloooking) is also explored wherein similar pixels are grouped with other similar pixels since it will be useful to differentiate the highly heterogeneous urban areas and possibly provide better results. This is done by checking the statistics of neighbouring pixels and evaluating their similarity by checking the distribution they follow. Here, 'multilooking' refers to spatially averaging, that is, a sample mean of the values of pixels within a window is taken. For the report, the terms multilooking and spatial averaging and used interchangeably.

Along with this, an exploration of the general ways in which PSs are used for detecting minute changes is done. For this research, PSs are detected from full-resolution images which serve as stable points, that is, points with a consistent backscatter over a long period of time. These stable points can be used to see changes in a timeseries that can be attributed to the disaster. This is a largely overlooked method that can be very useful in possibly detecting building-level damage.

There is no single method that is considered the best. The methods used for damage detection usually depend on the availability of data, the area under consideration and the type of change that is required to be tracked. On the other hand, the most commonly used damage maps are distributed by the National Aeronautics and Space Administration - Jet Propulsion Lab's (NASA JPL) Advanced Rapid Imaging and Analysis (ARIA) team, Copernicus Emergency Management Services (EMS) and Global Disaster Alert and Coordination System. The ARIA team, in fact, produces the Damage Proxy Maps (DPMs) operationally, that is, as soon as the disaster occurs and the images are available.

Nearly all of the methods that use amplitude and/or coherence as the primary parameters have bi- or tri-temporal change detection algorithms. For this research, a long timeseries is required to find the PSs. Hence, a long time-series of images is used to study data trends from three different parameters (amplitude, coherence, PSs) using the full resolution and multilooked images and a change detection method is used according to these requirements.

Table 2.3: Overview of different methods described in literature review. In the Spatial Resolution column, '–' refers to not enough data about the specific instrument used. In the Acquisitions column, the first number refers to the total number of images acquired followed by number of pre-disaster images plus number of post disaster images in brackets. When the brackets are not used, the study was not conducted in a post-disaster damage detection context. In the Parameters column, 'Both' refers to the fact that both amplitude and coherence were used in the particular study.

Authors	**Parameter**	**Satellite**	**Acquisition** [Days]	**Spatial Res.** [m]	**Comments**
Matsuoka and Yamazaki [34]	Intensity	ERS	9 (4 + 5)	30	Use a regression determinant score (2.2) which differentiates damaged from non-damaged. Relatively good agreement with ground truth. Thresholds have to be adapted according to region under consideration.
Matsuoka and Yamazaki [33]	Phase	JERS-1	6 (5 + 1)	30	Conclude that coherence is useful for classifying small damage levels.
Fielding et al. [20]	Phase	ENVISAT	5 (1 + 4)	–	Coherence is calculated using (2.14) to avoid overestimating it. Works best with low baselines and low SNR.
Hoffman [26]	Phase	ENVISAT	5 (2 + 3)	150	Used a coherence change index (2.3 to identify damage with thresholds assigned for different damage levels as in Table 2.3. Works best with short baselines.)
Yun et al. [53]	Phase	CSK and ALOS-2	3 (1 + 2)	3, 10	Coherence difference is calculated to produce DPMs. Good correlation to ground truth. Used operationally.
Matsuoka and Yamazaki [32]	Both	ERS-1 and 2	4 (3 + 1)	18	Coherence is used to detect small damage levels and amplitude used to detect heavy damage 2.4. Relatively good agreement with survey reports.
Stramondo et al. [44]	Both	Multiple sources	2 (1 + 1)	Varying	Use optical data along with SAR data to improve damage detection. Conclude that using coherence with optical images gives high accuracy.
Arciniegas et al. [3]	Both	ENVISAT, ASTER	3 (2 + 1)	15	Note that using coherence alone individually provides better results than using amplitude alone.
Gamba et al. [21]	Both	ENVISAT	3 (2 + 1)	30	Ancillary data is used in combination with SAR images. Note that using intensity alone produces better results, contradicting [3]
Trianni and Gamba [45]	Both	ERS	3 (2+1)	–	Proposed a fast unsupervised approach along with a slow (higher efficiency) supervised approach. Methods are imprecise when damage levels are relatively low.
Ferretti et al. [18]	PS	ERS	34	–	Exploit natural reflectors to track mm level motion. Final products are elevation and LOS velocity. Required long timeseries and high SNR. Best used in urban areas.
Berardino et al. [6]	PS	ERS	44	–	Introduced to deal with the problem of large baselines using SVD.
Ferretti et al. [19]	PS	RADARSAT	65	–	Applied to rural and urban areas by introducing the concept of distributed scatterers.

3 Methodology

This chapter describes the steps taken to process the Sentinel-1 imagery. The software Radar Interferometric Parallel Processing Lab (RIPPL) which was developed in the Department of Geosciences and Remote Sensing (GRS) of the Civil Engineering Faculty of TU Delft, is used to process the data. Currently, it is still in the development stage and has not been released publicly as of 8 August 2019. It is used for pre-processing the data set and facilitates further processing in Python by making the metadata available in convenient data formats. The data set is acquired from the Sentinel-1 satellite and made available by an open data policy by ESA. The process that leads to a damage map is three-pronged. The three parameters considered are Persistent Scatterers, spatially-averaged amplitudes and spatially averaged coherence.

It is important to use a reasonably long time series of images so that a statistical analysis can be done and more information about the pixels can be learnt from the stack. This is called multi-temporal analysis. A set of (≥ 30 images) spanning the pre-disaster period is considered, which contains variations due to seasonal changes or noise. This is compared with the post-disaster image immediately after the date of the disaster for any changes that can be attributed to the event.

3.1. The Algorithm

This section describes the steps taken to process the data. This includes pre-processing and calibration 3.1.1, Scaling and Outlier removal 3.1.2, Change detection 3.1.3 and Validation 3.1.4.

3.1.1. Pre-processing and Calibration

The dataset is downloaded from the Sentinel-1 database and pre-processed using RIPPL. This involves creating the stack of images, reading and storing the meta-data and geo-coding the images. The radar data are Single Look Complex (SLC) images which means that each image pixel is represented by a complex (I and Q) magnitude value and therefore contains both amplitude and phase information.

Firstly, the images need to be calibrated radiometrically, which is used to relate pixel values directly to radar backscatter of the scene [17]. A de-noising step or noise calibration is also applied along with the calibration. Look-up tables (LUT) are provided by ESA for this purpose. An illustration of the different backscatter scalings is shown in Figure 3.1. In this figure, β_o is the signal returned from distributed scatterers in the slant range coordinates. γ_o is the radar return or backscatter per unit area of the incident wavefront. Finally, σ_o is the radar return per unit area on the ground.

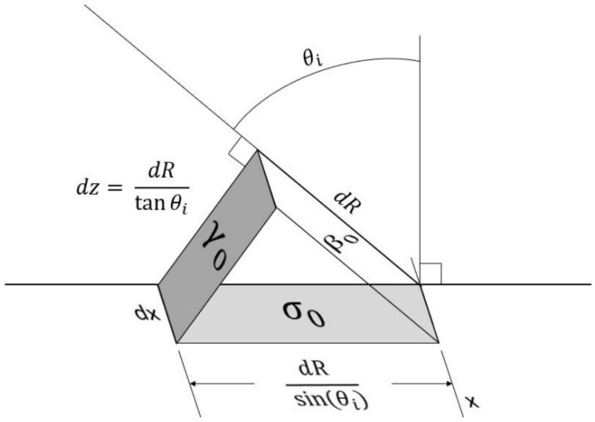

Figure 3.1: Schematic illustration of the various backscatter scalings: β_o, σ_o and γ_o. θ_i represents the local incidence angle; from R.K.Raney [39]

The radiometric calibration can be applied by the following equation.

$$\text{value(i)} = \frac{|DN_i|^2}{{A_i}^2}, \tag{3.1}$$

where value(i) can be β_o, σ_o or γ_o, and A_i is a calibration scaling factor for one of the desired outputs. DN_i refers to the digital number for a pixel i. Here, digital number refers the actual pixel values. There is a geometric impact on the backscatter signal due to the fact that pixels in the slant range cover different areas on the ground.

Similarly, a noise calibration is also done as follows:

$$\text{noise(i)} = \frac{\eta_i}{{A_i}^2}, \tag{3.2}$$

where η_i is a value from the noise LUT and noise(i) is defined similarly as value(i), and A_i is a scaling factor. Bilinear interpolation should be used for any pixels that fall between points in the LUT. Unfortunately, this step could not be applied due to time and memory constraints. Using calibrated data might provide slightly better results.

Since the radiometric calibration could not be applied, a version of it was implemented. The idea is that if there is any phase ramp or phase trends shown across the images, it will be removed. This is done as

$$\text{Calibrated amplitude} = \frac{A}{\sqrt{I}} \tag{3.3}$$

where A and I are amplitude and mean intensity values respectively for a single image.

3.1.2. Scaling and Outlier Removal

The images are then scaled in order to observe the general trends of the PSs over all the acquisitions. This is done by dividing the selected PSs by the mean of its values over all the acquisitions/days in the timeseries [40]. This helps the observations to be scaled consistently and helps to focus on the relationships between points over time. Additionally, any outliers are also removed. This is done by removing PSs from consideration that show abnormally large variations over the pre-disaster time-series.

3.1.3. Change Detection Algorithm

Surveying the literature provided various methods of change detection that rely of thresholding depending on the area under consideration [33], back-scattering coefficient [34], correlation coefficient [34] and gradient method [47]. For this particular application, the thresholding method and the gradient method were applied because these are particularly useful for a long multi-temporal application. The results of the gradient method are presented as it resulted in more accurate outputs.

The gradient method involves dividing the change in amplitude between co-disaster images by the maximum change between adjacent pre-disaster images for each pixel.

$$\text{gradient} = \frac{\Delta\sigma_{co-disaster}}{max(\Delta\sigma_{pre-disaster})} \tag{3.4}$$

where $\Delta\sigma$ represents the change in amplitude and co-disaster implies the images just before and just after the date of the disaster. If this gradient is greater than a threshold, then the point is considered to be changed due to the event. This threshold varies for different levels of spatial averaging. These 'changed' points are assumed to be damaged due to the disaster and overlayed on a map. The most widely available map that can be used by everyone considering the simplicity of its visualisations is Google Earth and hence it is chosen.

3.1.4. Validation

For verifying the correctness of the results obtained, it is usually compared to a ground truth survey. This usually has a list of all infrastructure and the extent of its damage in the area of interest. Ideally, this is verified with a ground survey after the disaster. An example of the reference map used is depicted below in Figure 3.3. This is provided by Copernicus Emergency Management System (EMS) [11]. It shows roads and buildings that have been classified as destroyed (red), highly damaged (dark orange), moderately damaged (light orange) and negligible to slight damage (yellow).

The entire methodology is illustrated by the flowchart in 3.2.

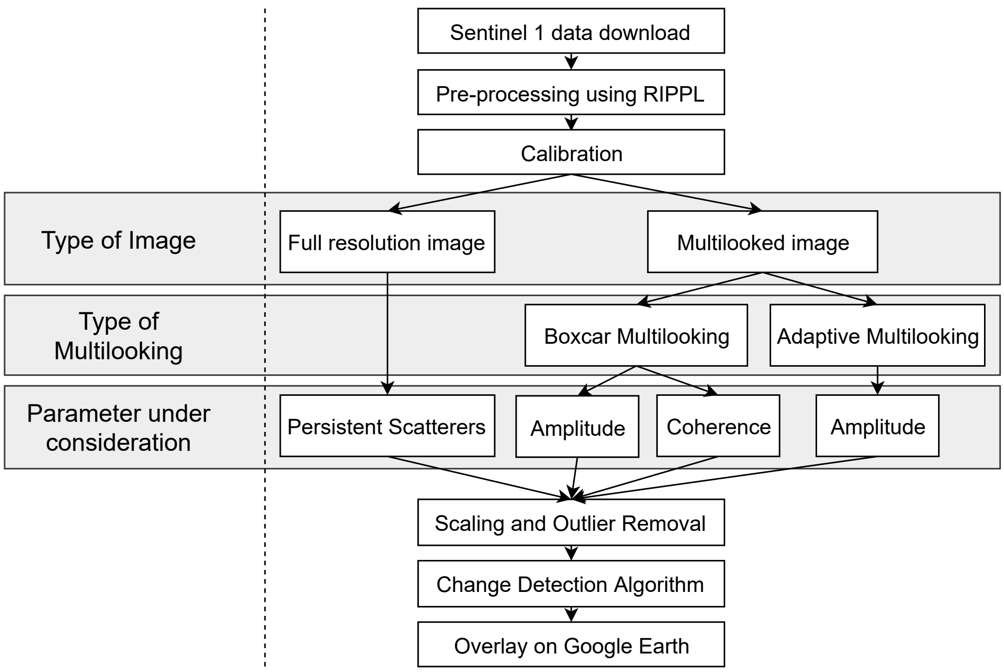

Figure 3.2: Block Diagram of flow of control for the methodology described in this chapter. After pre-processing and calibration using RIPPL, full resolution and multilooked images are used to study PSs, amplitude and coherence parameters. The final results are added to a .csv file which can be imported to Google Earth.

Figure 3.3: Grading Map By Copernicus Emergency Management System (EMS). The map describes any damage in infrastructure by means of colour-coded blocks with damage levels being - destroyed (red), highly damaged (dark orange), moderately damaged (light orange) and negligible to slight damage (yellow). It includes 'Crisis Information Points' where possible landslides, roadblocks, debris and temporary tents are represented. The map describes the situation as of 25 August 2016 and was produced on 31 August 2016. This is done by comparing post-disaster optical imagery with previous reference maps manually, without in-situ validation.

3.2. SAR Parameters

From the literature review, we learnt that there is tremendous value in using coherence and multilooked amplitude together since these signals react differently to different kinds of changes. It is also interesting to consider PSs in a context of sudden change detection for damage mapping since it comes with an added validity of a 'stable point'. So far, it has been largely overlooked for the purpose of building damage detection. The following subsections elaborate on each of these signals and the reasons for using them, the data models they tend to follow and they are manipulated for damage mapping.

3.2.1. Persistent Scatterers

PSs are points that are stable in phase, and by extension over certain conditions, stable in amplitude over a long period of time. They are usually corner reflectors and can be used very effectively to detect a change in urban areas. The PSs are chosen according to the method presented by Ferretti et al. [18]. To find stable points, one can consider the coherence as a parameter. The higher the coherence is over a large period of time, the greater the stability of the point. This process can get complicated since the phase has to be compensated for topography, atmospheric phase, terrain deformation, orbital indetermination, etc. Hence, another strategy is to consider the absolute backscatter (amplitudes) of the pixels which are largely unaffected by topography, atmospheric phase etc. under certain conditions. Ferretti et al. find that the amplitude dispersion index (D_A) is a good indicator of the phase dispersion in case of high SNR. The amplitude dispersion is defined as

$$D_A = \frac{\sigma_A}{m_A} \tag{3.5}$$

where σ_A is the standard deviation of the amplitude values and m_A is the mean of the amplitudes. The Figure 3.4 shows how well the amplitude dispersion substitutes for phase dispersion for varying levels of noise.

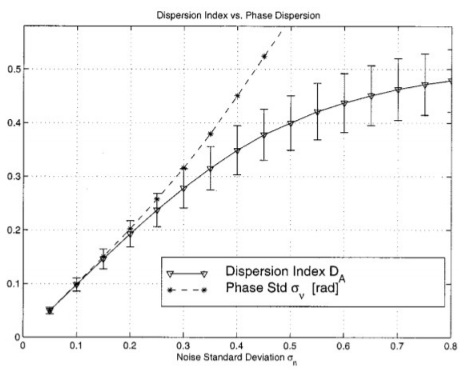

Figure 3.4: Amplitude dispersion index compared to the phase dispersion for varying levels of noise, from Ferretti et al. [18]. This shows the appropriate value of amplitude dispersion that can be chosen. 0.25 is an ideal value such that the amplitude dispersion is a good substitute for phase dispersion.

Thus, low amplitude dispersion values represent more stable scatterers. Generally, an amplitude dispersion value of around 0.25 is considered.

Data analysis was done to check the temporal distribution of the PSs and the consistency of assumptions. According to Ferretti [18], the distribution of amplitude values is given by a Rice distribution, which implies the presence of one dominant point scatterer in a background with several minor-subscatterers. The Rice distribution of amplitude values is given by the PDF

$$f_A(a) = \frac{a}{\sigma_n^2} I_o(\frac{ag}{\sigma_n^2}) e^{-(a^2+g^2)/2\sigma_n^2}, \quad a > 0 \tag{3.6}$$

where I_o is the modified Bessel function, g is the complex reflectivity, n is the circular Gaussian noise, with a power of σ^2. The shape of the Rice distribution depends on the signal to noise ratio (SNR), which is the ratio of g/σ_n. For lower SNR, the Rice PDF tends to a Rayleigh PDF and for high SNR, the Rice pdf tends to a Gaussian distribution.

Consider a data array $\mathbf{d} = [d_1, d_2...d_n]$ where n is the number of images in the stack excluding the post-disaster image. The data stacks $\mathbf{d}$ in the area of interest are checked against a Gaussian, Rice and Rayleigh distribution using the Anderson Darling test. For instance, in the first test, the null hypothesis is that the temporal data follows a Gaussian distribution and the alternate hypothesis is that the data does not follow a Gaussian distribution. The Anderson Darling test calculates a *test statistic*, which is the distance between the empirical 'cumulative cumulative distribution (CDF) functions of the sample (temporal data) and the reference (a Gaussian distribution) distributions. This distance is given by equation 3.2.2. If this test statistic is lower than a certain critical value at a significance level (chosen to be 1%), then the null hypothesis cannot be rejected. The critical values are distribution-specific and these values are provided in tables for some the most common distributions (normal, exponential, Weibull and some others).

The test showed that the null hypothesis cannot be rejected for nearly 84% for the temporal distributions in the area of interest, which means the data is Gaussian-like. The Rice and Rayleigh null hypotheses were rejected by the test. While the temporal distribution could be useful to formulate a change detection method which depends on the type of distribution, for the sake of uniformity in terms of applicability to different areas (where the distributions might not be Gaussian), such an approach has not been considered.

3.2.2. Spatially Averaged Images

Once the results from the full-resolution images are obtained, the amplitude images are then spatially averaged by a window of 2x6. This improves the SNR, helps in speckle-noise removal and considers points that are not PSs for possible damage. The marginal PDF of the amplitude values in a SAR resolution cell can be expressed as

$$f_A(a) = \begin{cases} \frac{a}{2\pi\sigma^2} exp(\frac{-a^2}{2\sigma^2}), & a \geq 0 \\ 0, & \text{otherwise} \end{cases} \tag{3.7}$$

This represents the Rayleigh distribution. Since the intensity is the square of the amplitude, the intensity is described by an exponential function.

Several empirical distributions have been used to characterise the statistics of SAR amplitude or intensity data such as Weibull, Fisher or log-normal PDFs. The empirical distributions come from the experience of analysing real data. To analyse the temporal distribution of the multilooked SAR amplitudes, the Anderson Darling test was used and the results, again showed that the temporal pixel data sets were Gaussian-like.

The steps of pre-processing and calibrating (3.1.1), scaling, outlier removal (3.1.2) and change detection (3.1.3) are applied to amplitude values of all the pixels over all images to find which areas are changed/damaged. These damaged pixels are then overlayed on a Google Earth as well.

Adaptive Spatial Averaging/Multilooking

Normal boxcar filtering is the most common method of filtering, which reduces the speckle noise at the expense of spatial resolution. However, for an urban area, it is counter-intuitive to use a boxcar filter considering the heterogeneity of the area. In this case, it is better to use an adaptive filter that averages similar pixels with other similar pixels, as in, averaging buildings with buildings, and trees with other trees.

Some adaptive approaches have been suggested in recent years. NL-InSAR [13] is an efficient method of adaptive multilooking but can only be applied to two images. Among the multitemporal approaches, Ferretti [19], in the paper where he introduces the SqueeSAR algorithm, suggested using the Kolmogorov-Smirnov test, a non-parametric statistical similarity test, to identify statistically homogenous pixels (SHPs) within a certain estimation window centred on the pixel under analysis in. Here, non-parametric means that no assumptions of the distribution of data vectors are made. Other similarity tests have been discussed where only the amplitude information is utilised [37]. Parizzi and Brcic [37] study three non-parametric and one parametric test and conclude that for a medium-sized stack, the Anderson Darling test was the most powerful non-parametric test, in comparison to Kullback-Leibler Divergence test and the Kolmogorov-Smirnov test. The Generalized Likelihood Ratio Test (GLRT) is a parametric test which can be very powerful for smaller stacks whose distribution is known.

The Anderson-Darling test has been used to check the similarity of pixels in the area of interest which are then averaged according to their similarity. Again, let us consider a data array $\mathbf{D} = [d_1, d_2...d_n]$ where n is the number of images in the stack excluding the post-disaster image. Within a sliding window, the temporal distributions of the data arrays for each pixel are checked against that of the central pixel in the window. As mentioned before, the Anderson-Darling test measures the distance between the empirical CDFs of the two

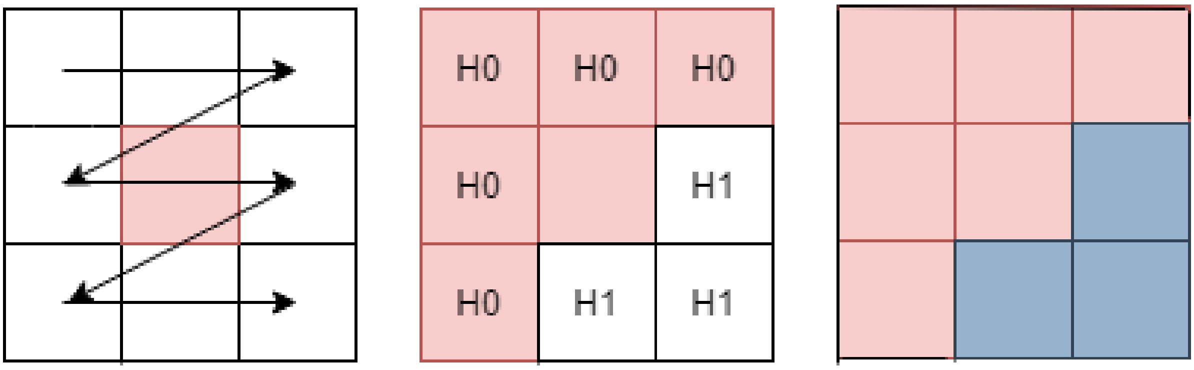

(a) Comparison of central pixel with other pixels in sliding window

(b) Check for similarity of distributions using Anderson Darling test

(c) Average similar pixels

Figure 3.5: The Adaptive Multilooking process is illustrated here. Each pixel within a multilooking window is compared to the central pixel to check for statistical similarity fof temporal distributions 3.5a. If a majority of the pixels are determined to be similar using the Anderson Darling test 3.5b, they are averaged together 3.5c. The ones dissimilar to the central pixel are ignored. This ensures that only similar looking topographic features are grouped together.

data arrays under consideration. The Anderson-Darling (1954) test is based on the distance

$$A^2 = n \int_{-\infty}^{\infty} \frac{(D_c(x) - D_i(x))^2}{D_i(x)(1 - D_i(x))} dD_i(x) \tag{3.8}$$

where n is the total number of images excluding the post-disaster image, D_i is the distribution of the pixel under consideration and D_c is the centre pixel of the sliding window against which all other pixels in the window are compared to.

Let us assume that H0 represents the hypothesis that the distributions of the pixels under comparison are similar, and H1 is the hypothesis that the two are different. If a majority of the pixels in the sliding window are similar to the centre pixel, the similar pixels are averaged and the dissimilar pixels are discarded. These averaged pixels become one pixel in the new grid. If a majority of the pixels in the window are dissimilar to the centre pixel, all the pixels in the window are averaged. In this case, it is at least as good as the boxcar multilooking method without losing any data. The sliding window is chosen to be 2x6 as before. Figure 3.5 illustrates the explanation.

This has been implemented in addition to the boxcar multilooking of amplitude values for comparison.

3.2.3. Coherence

Coherence is a measure of correlation between two SAR images. The complex coherence is defined as

$$\gamma = \frac{E\{y_1, y_2^*\}}{\sqrt{E\{|y_1^2|\}.E\{|y_2^2|\}}}, \tag{3.9}$$

where y_1 and y_2 are two zero mean circular Gaussian variables, E{} is the expectation or ensemble average and * denotes conjugation. The complex coherence $\gamma_{(M,S)}$ is calculated between the complex (single) master image M and complex slave image S. It is a function of both amplitude and phase.

For calculating coherence, multilooking (spatially averaging) is done using a sliding window of 2x6 over a non-multilooked image. Other multilook windows were also used for the calculation. Considering the size of the area of interest (AOI), windows of larger size meant that the AOI was reduced to too few pixels for effective localisation of damaged points. A smaller window size did not contain enough pixels for a reliable estimation of coherence values. Coherence values range between 0 to 1 and indicate how coherent or incoherent the co-registered images are. A sudden decrease in coherence is a good indicator of a change or damage in the area.

Once all the coherence were calculated for all master-slave pairs in the time-series, the change detection method explained in Section 3.1.3. Here, it is interesting to note that we would be considering the double difference in coherence to localise damaged buildings. the points detected as damaged are then overlayed on Google Earth.

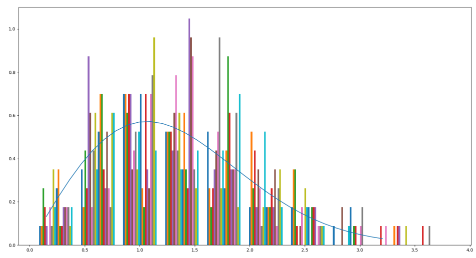

(a) Temporal distribution of PSs simulated as a Rice distribution along with a Rice fit for the purpose of finding expected behaviour of the system

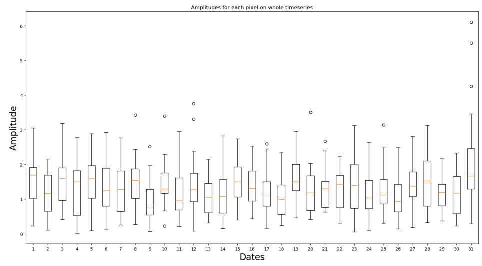

(b) Boxplot of the simulated timeseries with part of the distribution manipulated in the end to represent a 'change'

Figure 3.6: Plots showing simulated temporal distribution of PS amplitudes. Figure 3.6a shows the histogram of simulated Rice distributed values while Figure 3.6b depicts the variation in PS amplitudes over all the dates of the timeseries

3.3. Analysis Under Ideal Conditions

We have seen in the previous sections the damage mapping algorithm and the signals that are used for that purpose. In this section, basic analysis is done on how these signals behave under simulated ideal conditions to find the expected behaviour of the system under consideration.

3.3.1. With simulated change and simulated datasets

We saw that each of the parameters under consideration have their own temporal distributions. Let us consider the PSs first. According to Ferretti [18], PSs have a Rice distribution. For this little experiment, N points are simulated, which represent points on a map that may or may not be affected due to a disaster. Since we are working with timeseries, the points are actually vectors or an array of values that span a certain number of imaginary radar passes or epochs, say M, which is ideally 30 or more. Here, the M'th value represents the values of the post-disaster pixels. We end up with a two-dimensional array which is M-by-N, with the vector M simulated to be Rice distributed. This sets up our simulated radar dataset of PSs. The Rice distributed data points are shown in Figure 3.6a along with a Rice distributed fit. Each group of bars represents the N simulated points.

Now we try to simulate a 'change' in some of these points. Unfortunately, the way a natural or man-made disaster affects buildings is very complicated to describe purely in terms of a statistical model and is out of the scope of this research. We try to simulate a building being damaged by changing the M'th value of some of the N vectors in terms of the standard deviation of their preceding values.

Hence, some of the post-disaster pixel values are changed in increments of the temporally distributed data vector's standard deviation. For instance, a post-disaster pixel value is subject to 'damage' by changing it to 3 × standard deviation of vector M. This is tested with higher products of the standard deviation. The boxplots of all the simulated amplitudes along with their simulated changes in the last date are shown in Figure 3.6b. A boxplot consists of rectangular boxes with lines or 'whiskers' extending on each side. The rectangular box represents the interquartile range (IQR), which is the 25th to 75th percentile, of the values under consideration usually with a line in the middle to show the median of all values. The bottom whiskers represent the lowest data within 1.5 IQR of the lower quartile while the top whisker shows the highest data within 1.5 IQR of the upper quartile. Any data that is not part of this range is plotted as an outlier, represented by small circles above and/or below the whiskers.

When the algorithm described above is applied to this simulated dataset, there is no guarantee that the algorithm detects a 'change' if it is, say, 4 × standard deviation of vector m. The difference between the pre-disaster and post-disaster pixel must be higher than any other consecutive pixel difference in the rest of the time-series. A visual representation of the tests is shown in Figure 3.7. In Figures 3.7a and 3.7b, random Rice variables along with incorporated changes were generated over 5 different runs. Each of the bar groups represents the number of runs. We see that an increase in the product of standard deviation (n) generally causes a greater detection of change but there are cases when there is no detection as represented by values lower than a gradient of 1. For example, in Figure 3.7b there is an instance with an undetected change although that is not usually the case. We find that the point has to be a *global outlier*, that is, it has to deviate significantly from the rest of the data set. Figure 3.7c represents another test done with greater products of standard deviation and 50 runs. We see that at n=8, there is no point that goes undetected as changed. At this point though,

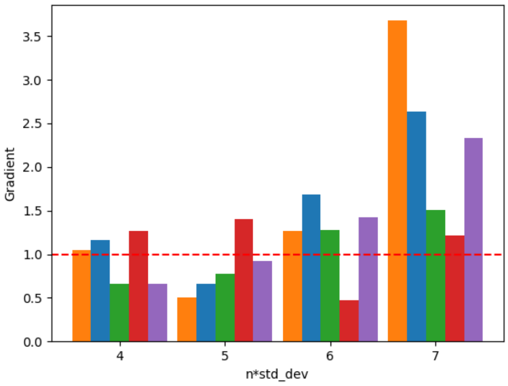

(a) Bar graphs of 5 runs of randomly generated Rice distributions with varying levels of changes.

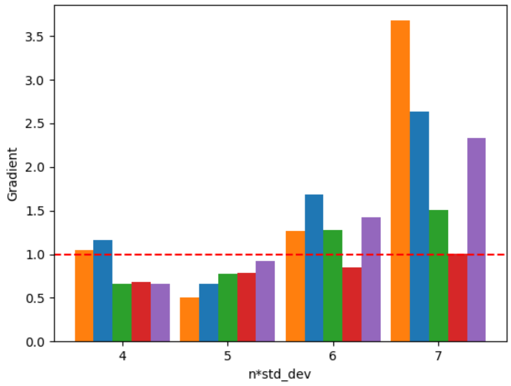

(b) Bar graphs of 5 more runs of randomly generated Rice distributions with varying levels of changes.

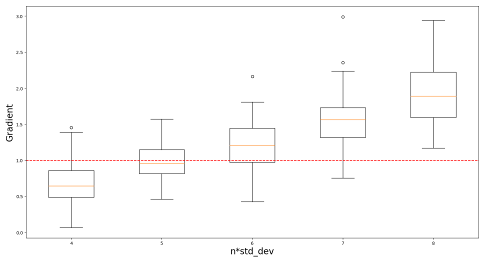

(c) Boxplots depicting expected behaviour of change detection algorithm by varying the extent of change in terms of products of standard deviation over 50 runs.

Figure 3.7: Plots describing the extent of change required for the algorithm to detect the change.

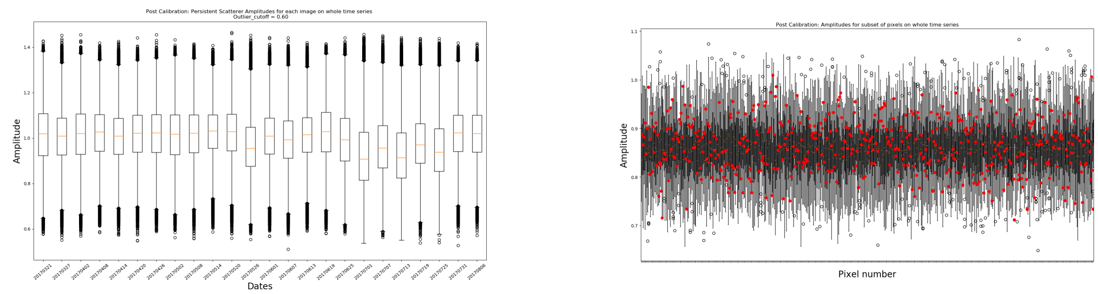

(a) Boxplot showing PS amplitudes over the timeseries.

(b) Boxplots showing PS amplitudes over a subset of all of the pixels in all images.

Figure 3.8: Boxplots showing amplitudes PSs when no known change has occurred in Mexico City

8 × standard deviation is already a global outlier. This also means that the change detection method is inordinately dependent on whether the pre-disaster image follows the general trends of the whole time-series so as to not skew the results.

On the flip-side, for the points that followed the same temporal Rice distribution for the whole timeseries, or in other words had no simulated change, the algorithm did not detect any damage and hence avoided false alarms. This, however, might not always be the case with real data. This is tested in the next subsection.

A similar procedure is done for the multilooked amplitudes that ideally follows a log-normal distribution and, for the sake of convenience, a Gaussian distributed coherence signal is considered. Both of these confirm the previous findings from the PSs. It also shows that the algorithm seems to be independent of the type of distribution of the dataset of each parameter.

3.3.2. With no change and real datasets

In the previous subsection, we have seen how the algorithm behaves with on a simulated dataset with simulated changes in the post-disaster image. Here, the actual Sentinel-1 dataset is used to see how the algorithm behaves under no change or damage. This is done to see how many false positives are produced, that is, there is no real change, but the algorithm detects a change. Ideally, the number of false positives is very low or negligible. But we also do not want to set our thresholds so low that the algorithm behaves very conservatively and produces true negatives (a real change that is not detected by the algorithm). In this particular application, the presence of a low number of false alarms is, in a sense, forgivable. So the thresholds must be a balance between the lowering false positives and eliminating true negatives.

For this, a set of images are chosen with no known change or disaster occurring over the entire timespan. Mexico City is an area of interest in the following Chapter where the algorithm is tested during the 2017 Puebla earthquake. The same area is used in this sub-section, but with a dataset that precedes the date of the earthquake.

The algorithm is applied as described in section 3.1. The same thresholds are also used that have been used for finding the actual points of damage in the results section for Mexico City. For the case of the PSs, Figure 3.8 shows the boxplots of amplitudes of PSs when no known change has occurred. In Figure 3.8a, we see the general trends of the amplitude values after scaling and outlier detection, over all the days of the timeseries. Here, each box represents the range of amplitude values acquired over a single date. We see that these are largely even and are around the same range of values. Figure 3.8b shows the amplitudes of PSs over a subset of all the pixels. Each rectangular box represents the range of PS amplitudes of a single pixel for all of the dates. The red dots represent the values from the last date, which has no change. In case of a drastic change, these red points are expected to be among the outliers in the boxplots but that is not the case. In the end, no points of change are detected, which is accurate since no known damage occurred. The multilooked amplitudes show a similar result. The plots showing the general trends of multilooked amplitudes over the timeseries are given in Figure 3.9.

In the case of the coherence signal, specifically, 24 image pairs were used between the dates of 21 March 2017 and 6 August 2017. There were 12 points that were shown to be changed, which is a relatively few number of false positives as shown in Figure 3.10. Let the subset of false positives be represented by D_{FP}. We could also speculate that there could have been construction work that was happening in points depicted by D_{FP}. Also, none of these points were the same points detected as damaged during the actual disaster. Let these

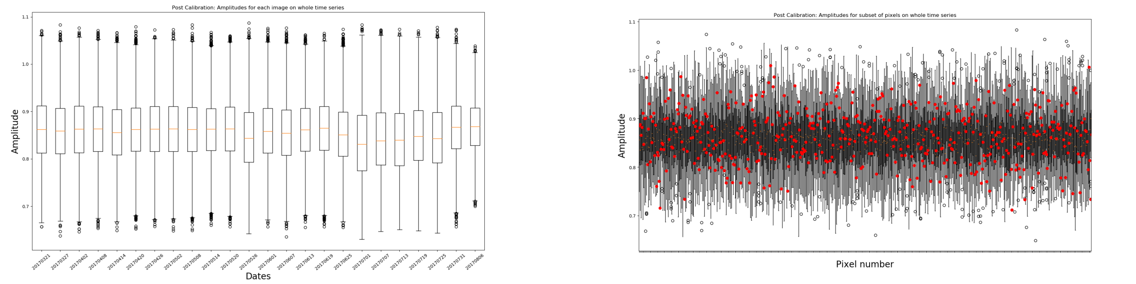

(a) Boxplot showing multilooked amplitudes over the timeseries.

(b) Boxplots showing multilooked amplitudes over a subset of all of the pixels in all images.

Figure 3.9: Boxplots showing the behaviour of multilooked amplitudes when no known change has occurred in Mexico City

points be represented by D_{TP}. This means that those points, D_{TP}, can be attributed solely to the disaster.

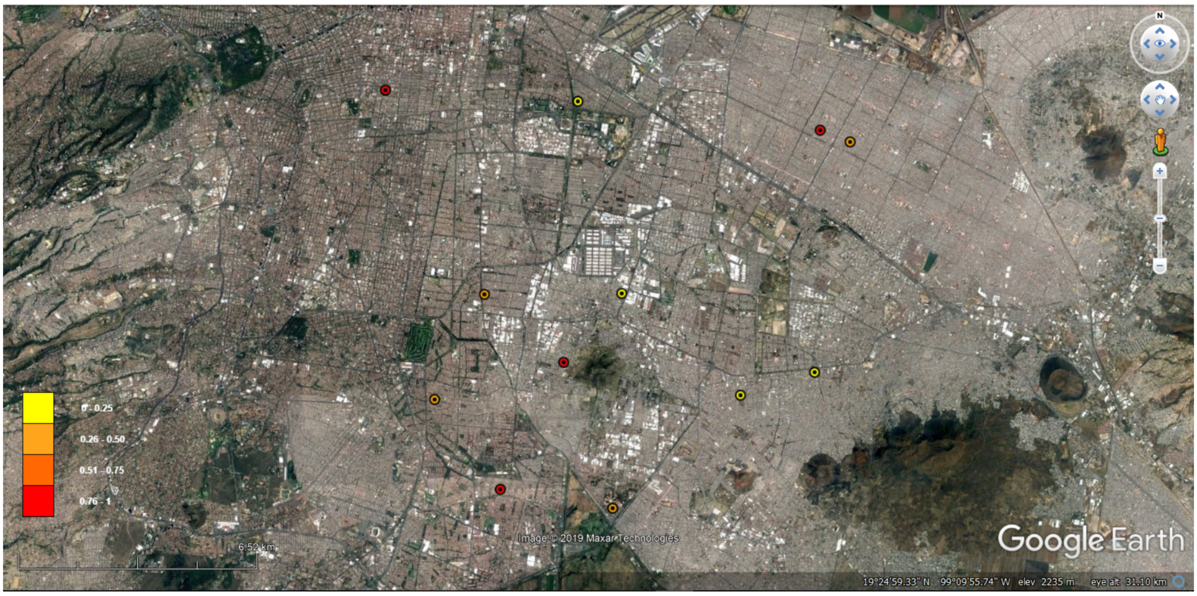

Figure 3.10: Results of applying algorithm to coherence signal acquired from Mexico City with no known change occurring during the timeseries.

The real test of the algorithm is given by how many true positives it produces with the real dataset, that is, it should detect if not all, most of the damaged areas attributed to the disaster. Additionally, it should have a low number of true negatives. This is tested in the next Chapter by applying the algorithm to the two main areas of interest - the town of Amatrice in Italy and the city of Mexico, both of which were heavily impacted by powerful earthquakes.

4
Results

In this chapter, the results of the algorithm explained in the previous chapter, will be described for multiple areas of interest. Specifically, it is applied to two areas that were struck by earthquakes. The methodology is analysed on its ability to determine the damaged points correctly and the interpretability of the resultant map. This is done by keeping track of the number of points correctly determined as damaged (true positives) and false positives. The percentage of unique points correctly determined to be destroyed by each parameter is analysed. This gives us information about the usefulness of using the different parameters and the advantages and disadvantages of each. The percentage of points correctly classified as damaged by multiple parameters are also analysed. This provides an added validation that the area is damaged.

Usually, the accuracy of damage maps is evaluated by comparison to the ground truth data. Unfortunately, this information was not available readily. However, Grading Maps are provided by Copernicus Emergency Management Services (EMS) - Mapping which consists of mapping services funded by the European Commission. They manually compare high-resolution optical pre and post-disaster images to check for building damage.

The methodology was applied in two areas of interest - Amatrice, Italy during the 6.2 magnitude Central Italian earthquake in 2016 and Mexico City, Mexico, during the 7.1 magnitude Central Mexico earthquake in 2017. The following section details the results found for Amatrice, Italy.

4.1. Amatrice, Italy

An earthquake of magnitude 6.2 occurred in the hilltop town of Amatrice in Italy 4.1. The earthquake struck on the 24th of August, 2016 at 03:36:32 CEST with no warning or weaker foreshocks. The epicentre was located 45 km north of L'Aquila, the capital of the Abruzzo region. The earthquake resulted in the fatality of 299 people, 234 of which were in Amatrice.

The dataset selected for processing spanned 30 images over 06 June 2015 to 21 August 2016, with the post-disaster acquisition on 2 September 2016. The interval between two consecutive images is 12 days.

The satellite image from Google Earth of Amatrice (to the right) and the nearby lake, Lago di Scandarello, is shown in Figure 4.1. The radar image of the same area is shown in Figure 4.2. The image is upturned due to the viewing angle of the satellite (descending). The images are pre-processed in RIPPL and then the PSs are selected. These PSs are obtained once the amplitude dispersion threshold is set to 0.26 as shown in Figure 4.3. This particular value is chosen since Amatrice is not a densely built area and to get enough number of

Table 4.1: Overview of the parameters of the satellite imagery used for analysing the 2016 Central-Italy earthquake.

Pre-Disaster Acquisition Span	06 June 2015 to 21 August 2016
Disaster Date	24 August 2016
Post-Disaster Acquisition	02 September 2016
Repeat Cycle	12 days
Orbit Number	22 (Descending)
Pre-disaster stack size	30

Figure 4.1: Google Earth Image of The central-Italian town of Amatrice along with the lake Lago di Scandarello to the west.

PSs to represent built structures of the town appropriately. A total of 309 PS points are obtained, mostly in the north-west part of the city, where the bulk of the buildings are situated. The points almost always follow the outline of buildings with a slight shift in certain cases due to the height of the building.

The PS points are scaled and the outliers removed as explained in section 3.1.2. Figures 4.4a shows the boxplot of the scaled amplitudes of all pixels over the pre-disaster time series. Figure 4.4b shows the boxplot of the scaled amplitudes of all pre-disaster images for a subset of all the PS points. Figure 4.4b is basically the transpose of Figure 4.4a. This plot depicts the general characteristics and trends of the amplitude values just before the disaster occurs. On 21st August, 11th February and 18th January 2016, we notice that there is a drop in the amplitude. However, most of the amplitude values are centred around 0.75 and 1.25.

The amplitude values after outlier removal are shown in Figure 4.5a and 4.5b. There is a marked reduction in the number of outliers. In Figure 4.5a, the largest variation in amplitude values are on 02nd September 2016, which represents the post-disaster acquisition. In 4.5b, the red points represent the values of pixels from the post-disaster image. These points make up most of the outliers in the individual box plots. This is in line with the idea that most of the amplitude variations occur after a drastic change and in this case, the change can be attributed to the earthquake.

Once the scaling and outlier removal is done, the change detection method is applied so as to find the damaged points. This is done using the change detection method described in 3.1.3. The gradient output is normalised to a range between 0 to 1 and colour coded over a gradient from yellow to red representing low damage to highly damaged, pictured by coloured circular dots overlayed on Google Earth. Since the output is in the form of a .csv file containing information about the damage level, latitude and longitude, it can be easily imported to Google Earth or QGIS for visualisation.

The results from the algorithm need to be validated using some reference map. This is provided by Copernicus Emergency Management System (EMS) [11]. The grading map shown in Figure 3.3 is produced by comparing high-resolution optical pre- and post-disaster imagery manually and checked for changes in urban structures and areas of rubble. The EMS map generated 7 days after the earthquake and shows roads and buildings that have been categorised as destroyed (red), highly damaged (dark orange), moderately damaged (light orange) and negligible to slight damage (yellow).

The results of the methodology applied to PSs obtained from full-resolution images is shown in Figure 4.6. Most of the damage is localised over the north-west part of the town according to the reference map. Most of the points classified as damaged according to the PSs parameter are concentrated here as well. Although not every damaged building in the north-west part of the city is recognised as damaged, the current results match well with the grading map. It does well in identifying clusters of areas that are damaged. One should also consider that the backscattering effect depends on the viewing angle of the satellite and which parts of the building have been battered. It is possible that some buildings that were damaged were not picked up

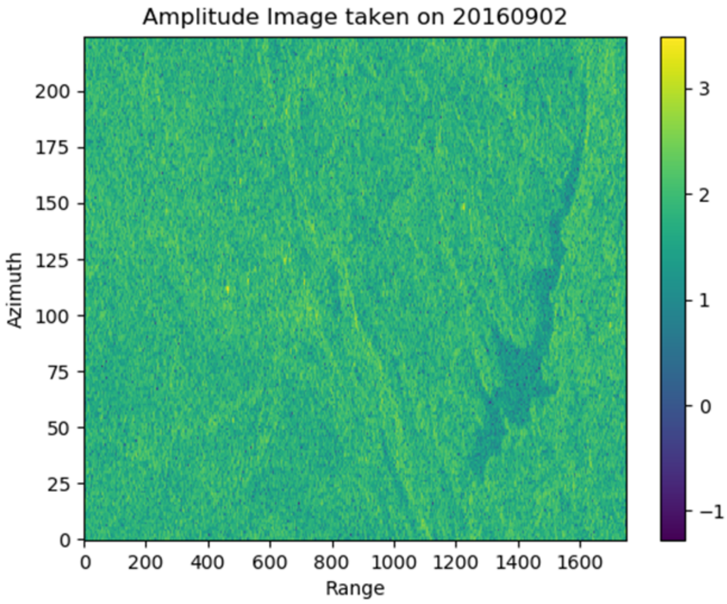

Figure 4.2: The radar image showing amplitude backscatter of Amatrice along with the lake, acquired on 2nd September 2016

Figure 4.3: PSs in Amatrice with $D_A = 0.26$. The green dots represent the PSs and the grey blocks represent buildings. The PSs roughly follow the outlines of the buildings with a slight shift in some cases due to the height of the building.

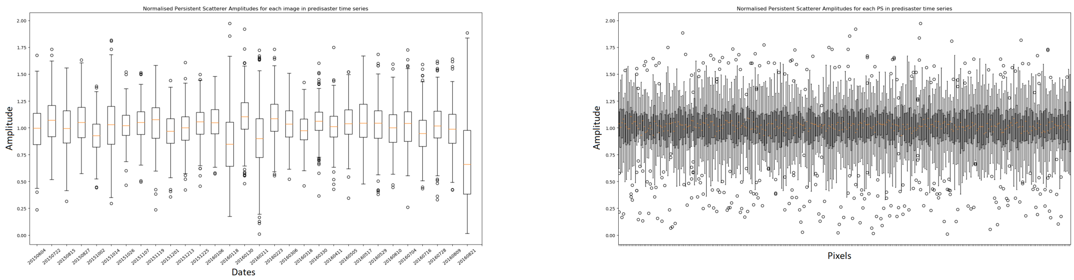

(a) PSs Amplitudes over pre-disaster timeseries after scaling

(b) PSs Amplitudes over subset of PSs after scaling in pre-disaster timeseries

Figure 4.4: The images show boxplots that describe the general trends of the scaled amplitudes of PS over the pre-disaster time period for the region of Amatrice.

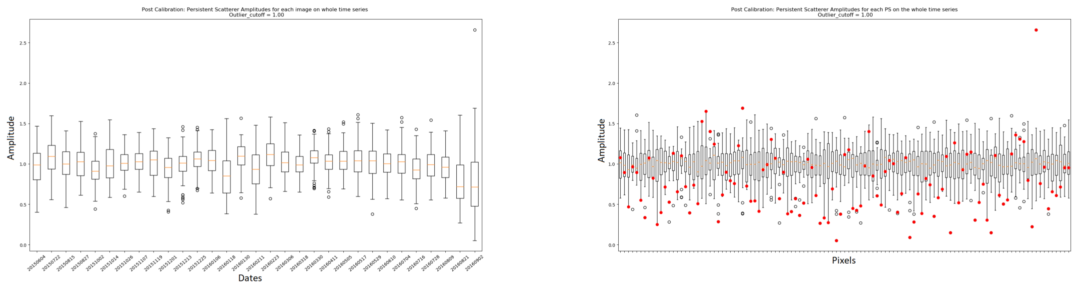

(a) PSs Amplitudes over whole timeseries after scaling and outlier removal

(b) PSs Amplitudes over subset of PSs after scaling and outlier removal in whole timeseries.

Figure 4.5: The images show boxplots of PS amplitudes after outlier removal and describes how the post-disaster image shows marked variations from the pre-disaster timeline for the region of Amatrice.

due to the viewing angle of the satellite.

A total of twenty-two points are identified as damaged by the PS parameter, which is a little over 7% of the total number of PSs that were identified initially. There are four points that are unaccounted for, and show up as false positives, mostly in the middle eastern section of the town. That means that 81% of all the identified points were correct.

Once the initial run using the full resolution images are processed, the images are spatially averaged using a 2x6 multilooking window and the processes are implemented as described in Section 3.2.2. The results of the methodology applied to spatially averaged images are as shown in Figure 4.7.

We notice that in general, this method classifies a lot more points, specifically seventy-six points after vegetation masking, as damaged. This approach does not catch some of the points that using PSs does, especially in the western part of the city but it particularly identifies areas that the PS parameter misses, such as the setting up of relief tents (represented by blue cones) towards the south and south-eastern part of the town as shown in 4.7. There are several outliers present outside of the city in vegetated areas, which can be removed by a vegetation mask. After the vegetation mask is applied, there are around eight points that are unaccounted for. There is also a curious cluster of points in the eastern end of the city which is not classified as damaged in the EMS maps. A closer investigation in the Google Earth historical images reveals that it was probably used as a car park soon after the disaster occurred. This comparison is shown in Figure 4.8. Therefore this particular parameter has an accuracy of 89.4% when applied to Amatrice region.

Although the normal boxcar multilooking method gives pretty accurate results, there are a lot of outliers in the areas with vegetation. These have been removed using a mask. In comparison, the adaptively multilooked amplitude values perform much better in terms of reducing false positives in the vegetated areas. The adaptively multilooked values also did not need the calibration step. The results using adaptively multilooked amplitudes match the general pattern of the boxcar multilooked results but it does not identify all of the points that boxcar multilooking does. Out of a total of forty points determined to be damaged, there are five false positives that are unaccounted for, resulting in an accuracy of 87.5%. The results of the adaptively multilooked images are shown in Figure 4.9.

Next, we find the coherence of all consecutive image pairs in the stack. Figures 4.10a and 4.10b illustrate

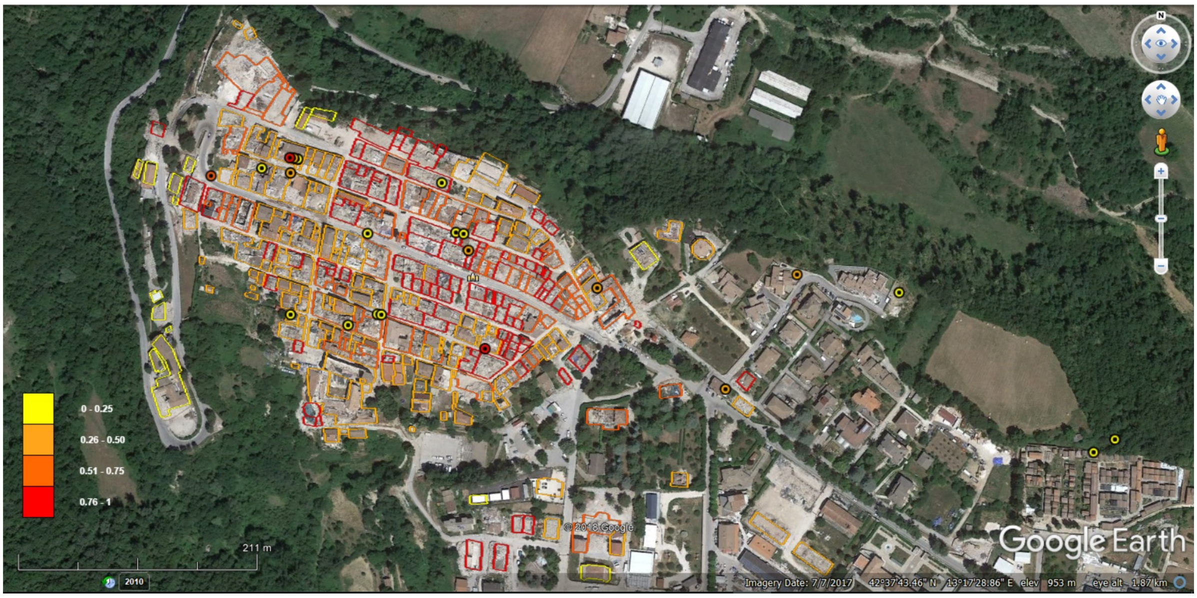

Figure 4.6: Results of the methodology applied to PSs obtained from full-resolution images for the city of Amatrice after the M6.2 2016 Central-Italy earthquake

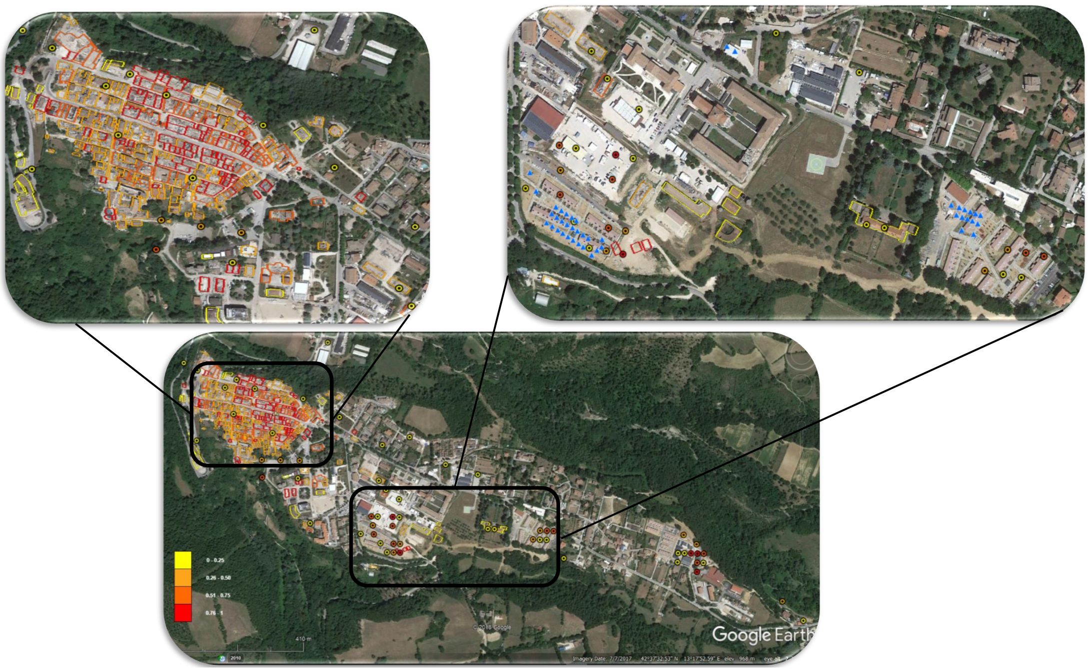

Figure 4.7: Results of the methodology applied to pixels in boxcar multilooked (2x6) images for the city of Amatrice after the M6.2 2016 Central-Italy earthquake. To the top-left, the western part of the town which sustained the most destruction is zoomed in. To the top right, a magnified image of the central part of Amatrice is shown. This is where most of the temporary relief tents were set up, which is represented by blue cones. These appearance of the tent post the earthquake has been captures by the change detection algorithm.

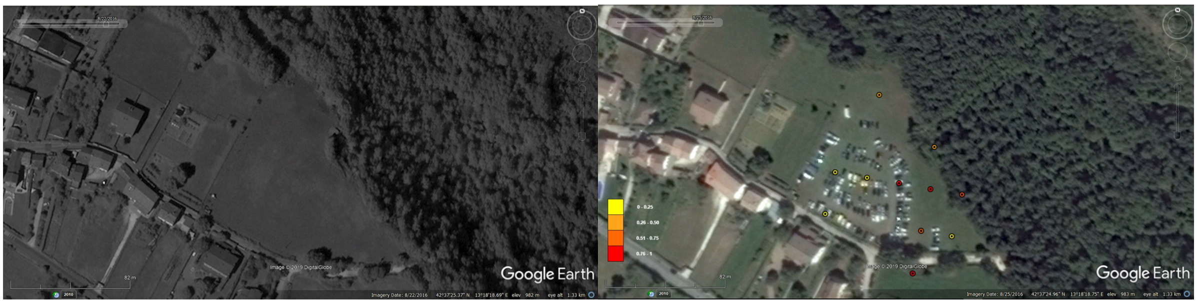

(a) Eastern part of Amatrice before the earthquake on 22 August 2016 (b) Eastern part of Amatrice after the earthquake on 25 August 2016

Figure 4.8: Eastern end of Amatrice which was used as a car parking area after the earthquake as observed from Google Earth historical images. This change is also picked up by the methodology used with boxcar multilooked (2x6) images.

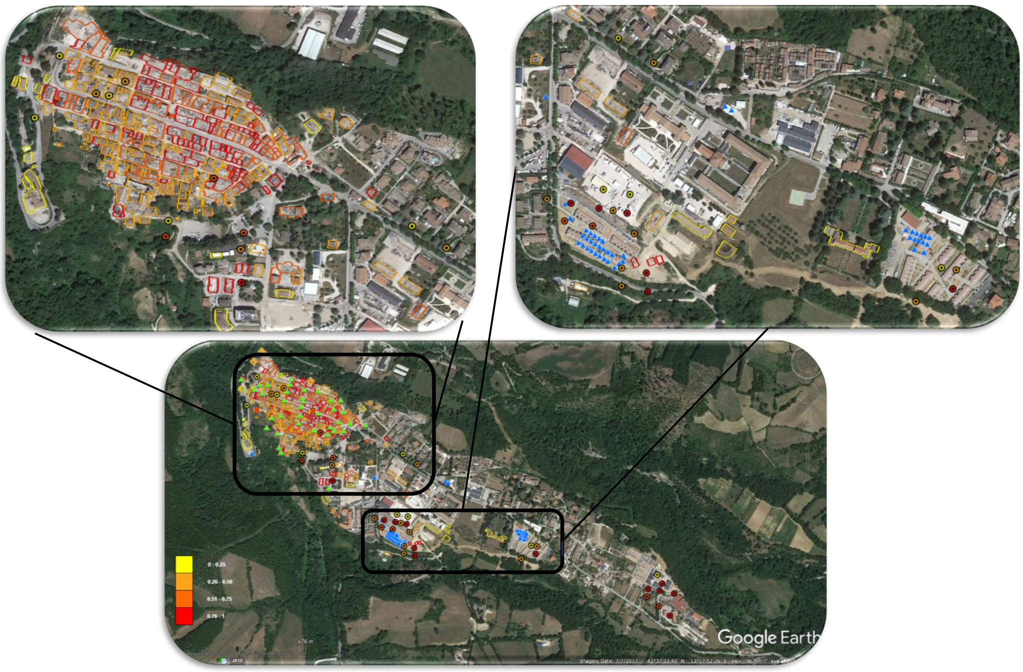

Figure 4.9: Results of the methodology applied to pixels in adaptive multilooked (2x6) images for the city of Amatrice after the M6.2 2016 Central-Italy earthquake. An enlarged image of the historical, western part of Amatrice is shown on the top left along with the relief tents area which is magnified on the top right side of the image.

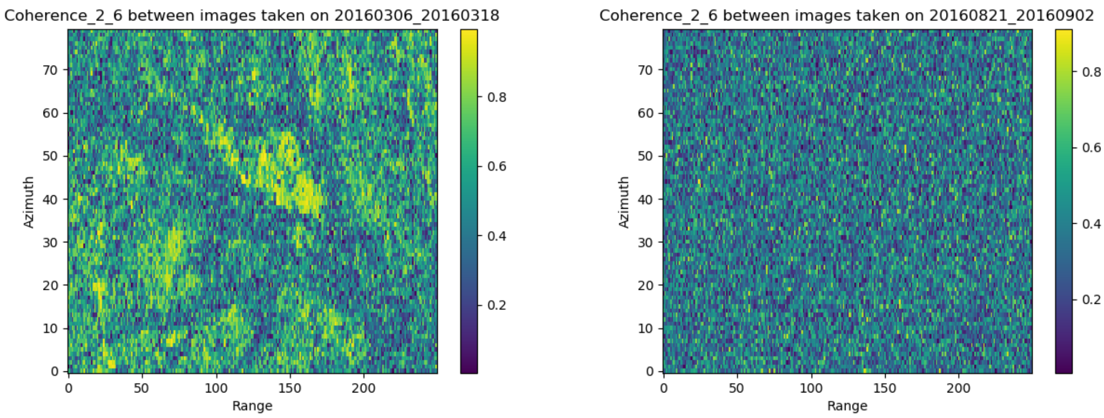

(a) Coherence of pre-seismic image pair

(b) Coherence of co-seismic image pair

Figure 4.10: Coherence comparison betweeen pre- and co-seismic image pairs. The average coherence drastically reduces in the co-seismic image pair due to the earthquake.

the coherence of a pre-disaster image pair and the co-disaster image pair over the town of Amatrice. There is a drastic difference between the coherence of the two image pairs. The brightest part of the Figure 4.10a is the town of Amatrice. The change detection method is applied to these image pairs to find the damaged areas. The results of this are shown in Figure 4.11.

We see that although there are not many pixels classified as damaged, it provides correct, unique damaged points that were previously classified as not damaged using the other parameters as shown in Figure 4.11. Out of a total of 11 points identified as damaged, most of the pixels are correctly classified, with the exception of a few (two) points that are unaccounted for. A mask is applied to the results to ignore points in vegetated lands. Therefore, this method shows an accuracy of 81%.

Considering the results from all parameters collectively, we see that the resultant map identifies most of the damage to the city as shown in Figure 4.12. This figure zones in on the most damaged part of the town to represent the points identified by using each parameter. Considering the correctly classified points, the PSs and multilooked coherence in addition to the multilooked amplitudes provides no repetitions except one, that is, nearly all the points classified as damaged by each method are unique. The one repetition occurs in the parking lot towards the eastern end of the city, with both multilooked amplitude and coherence identifying the area as changed. This implies that each parameter has been useful in picking up varying levels of damage. In the case of Amatrice, all the parameters performed equally well with a total true positives of about 87% after vegetation masking. Table 4.1 shows the accuracy of the results of the methodology when the parameters are used individually as well as the combined accuracy of all three parameters used together.

Table 4.2: Table showing the accuracy of the results of the methodology used for Amatrice in Italy, which includes the number of points detected a damaged and the percentage of those correctly determined to be damaged (True Positives)for parameters used, individually and combined

	PS	Amplitude	Coherence	Overall
No. of points detected	22	76	11	109
True Positives	81.81%	89.47%	81.81%	87.15%

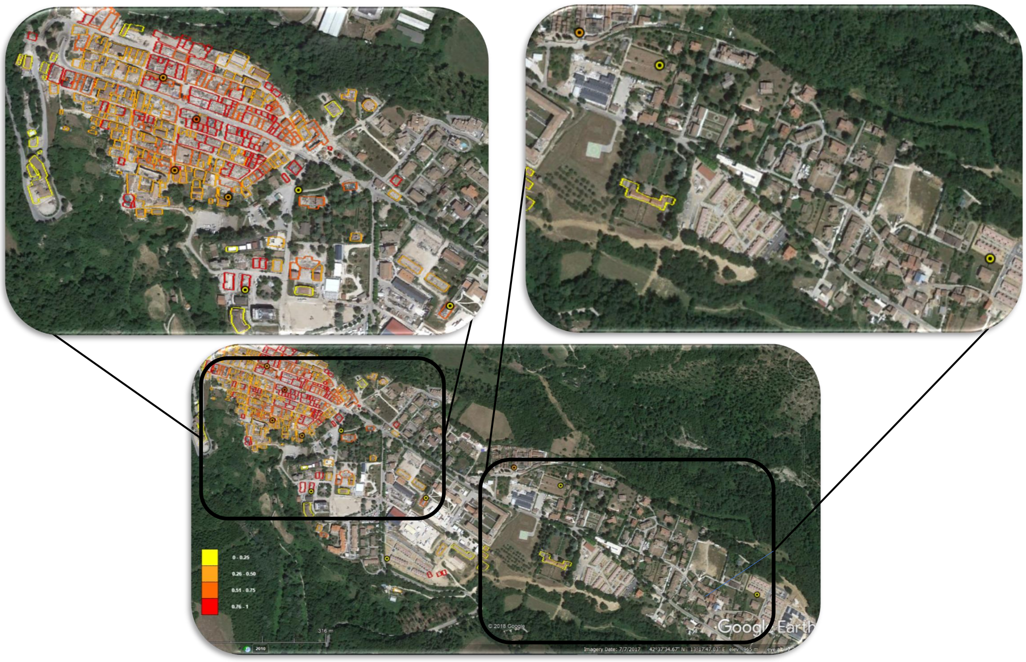

Figure 4.11: Results of the methodology applied to coherence values in boxcar multilooked (2x6) images for the city of Amatrice after the M6.2 2016 Central-Italy earthquake. To the top left, an enlarged image of the eastern part of town is shown along with a zoomed-in picture of the central-eastern part of town. Although the coherence parameter characterises a lot fewer points as damaged, it identifies new, unique points that other parameters don't.

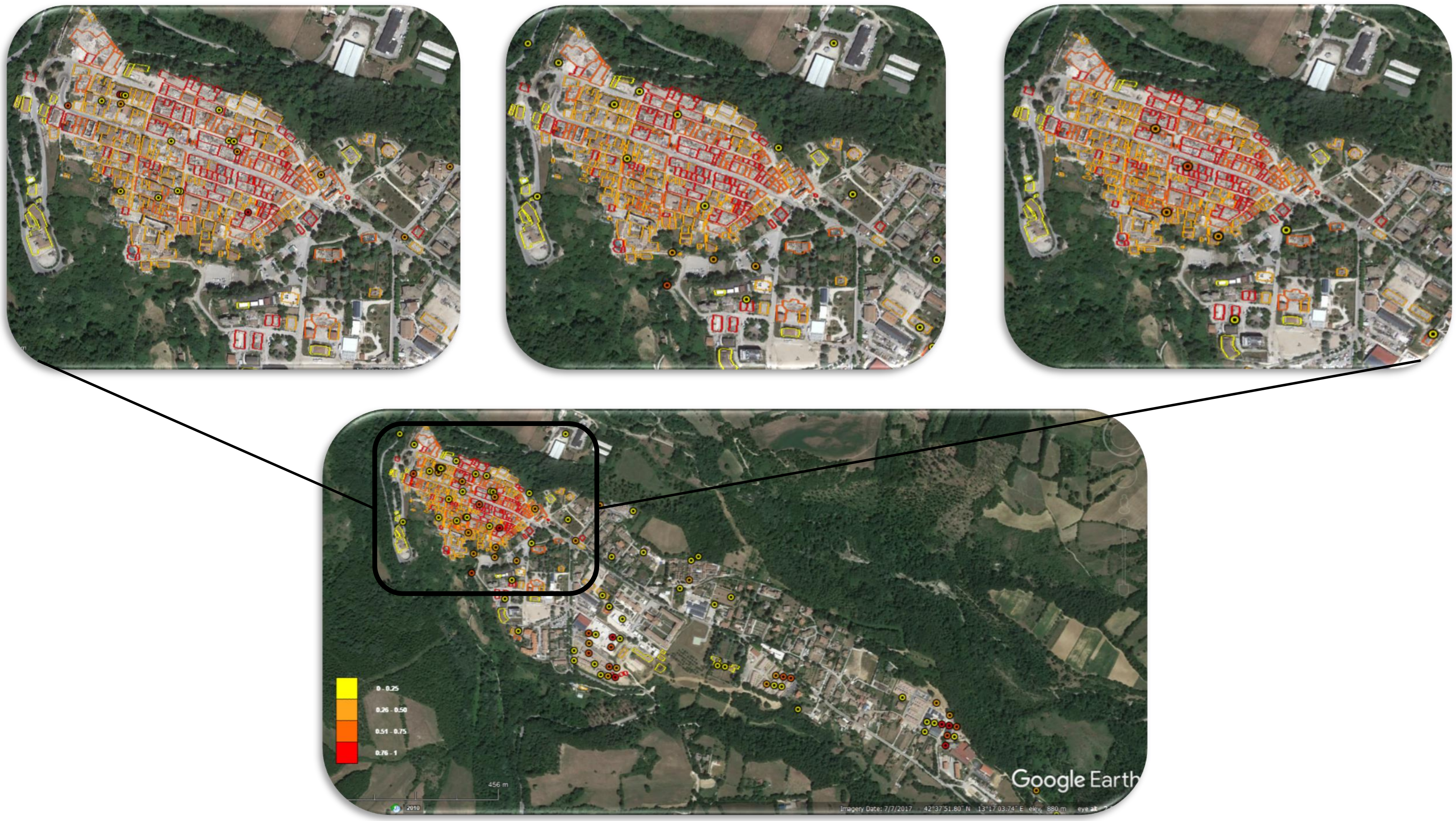

Figure 4.12: A magnified image of the historical part of Amatrice is shown, which consists of the Western part fo the city, after the M6.2 Central Italy earthquake. The image below shows the results from all the parameters together in one collective map. We see that most of the clusters of building are correctly characterised as damaged. To see the contribution of each parameter to this collective map, the call-outs are pictured. To the top left, we see the results from the PSs. In the middle, the multilooked amplitude results are shown and to the top right, the coherence results are portrayed. Each parameter significantly contributes to the results with a total true positive rate of 83%.

4.2. Mexico City, Mexico

On 19th September 2017 at 13:14 CDT, Mexico City and the nearby state of Puebla were struck by a $M_w 7.1$ magnitude earthquake, widely known as the 2017 Puebla earthquake. Coincidentally, it happened on the 32nd anniversary of the 1985 Mexico City earthquake, which killed around 10,000 people. The Puebla earthquake caused most of its damages in Puebla and the Greater Mexico City area. According to reports, 44 buildings collapsed [46]. A total of 370 fatalities were caused directly by the earthquake and related building collapses, including 228 in Mexico City [9] with more than 6,000 others injured [1].

Table 4.3: Overview of parameter of the dataset used for the 2017 Puebla earthquake

Pre-disaster acquisition span	21st March 2017 to 17th September 2017
Disaster Date	19 September 2017
Post-Disaster Acquisition	23 September 2017
Repeat Cycle	6 days
Orbit Number	143 (Descending)
Pre-disaster stack size	30

The dataset is downloaded from the Sentinel 1 open-access database. The time series consists of 30 pre-disaster images from 21st March 2017 to 17th September 2017, with the post-disaster image acquired on 23rd September 2017, four days after the earthquake struck. Each image is spaced 6 days apart from the preceding and succeeding image. The radar image of Mexico City is shown in Figure 4.14 along with the Google Earth coloured satellite image in Figure 4.13. The radar image is inverted since the viewing angle is descending.

Figure 4.13: Google Earth Image of Mexico City

First, we pre-process the dataset in RIPPL followed by finding the PSs by setting an amplitude dispersion threshold of 0.25. This value is chosen since Mexico City is densely populated with buildings constructed very close to each other. A total of 193213 PSs were found in the area of interest as shown in Figure 4.15. The PSs also act as a vegetation and water-body mask, since it clearly demarcates the lakes and parks from the buildings.

The scaled amplitude for all of the PSs over the pre-disaster time-series of imagery is shown in Figure 4.16a. The transpose, which represents the amplitudes of images for a subset of all the pixels, is shown in Figure 4.16b. These boxplots are constructed to show the general trends of the PSs and images before the earthquake occurred. The amplitude trends observed are largely even except in the image immediately before the disaster (17th September 2017), as in Figure 4.16a. The cause for this perturbation is not confirmed. Inclement weather conditions can sometimes cause disturbances in the radar signal but the 23 September 2017 checked out to be sunny and relatively cloudless for Mexico City. It also is not a processing error since

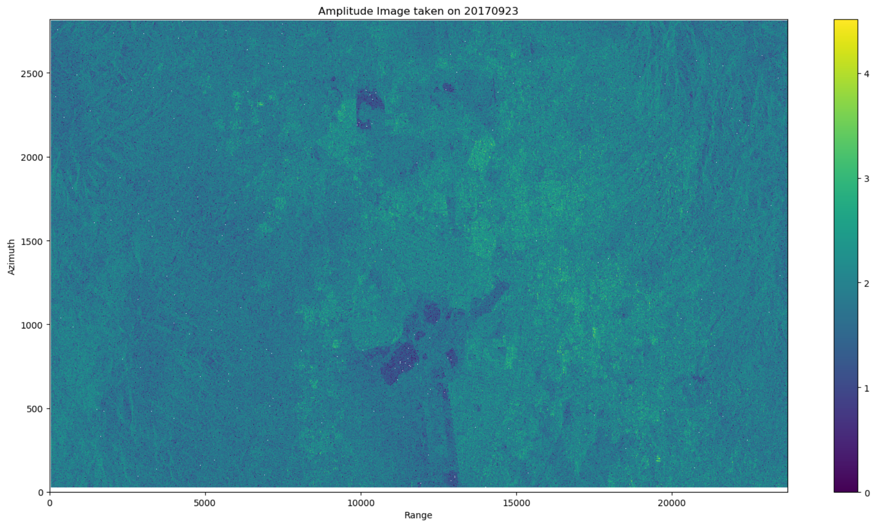

Figure 4.14: Radar Image showing amplitude backscatter of Mexico City

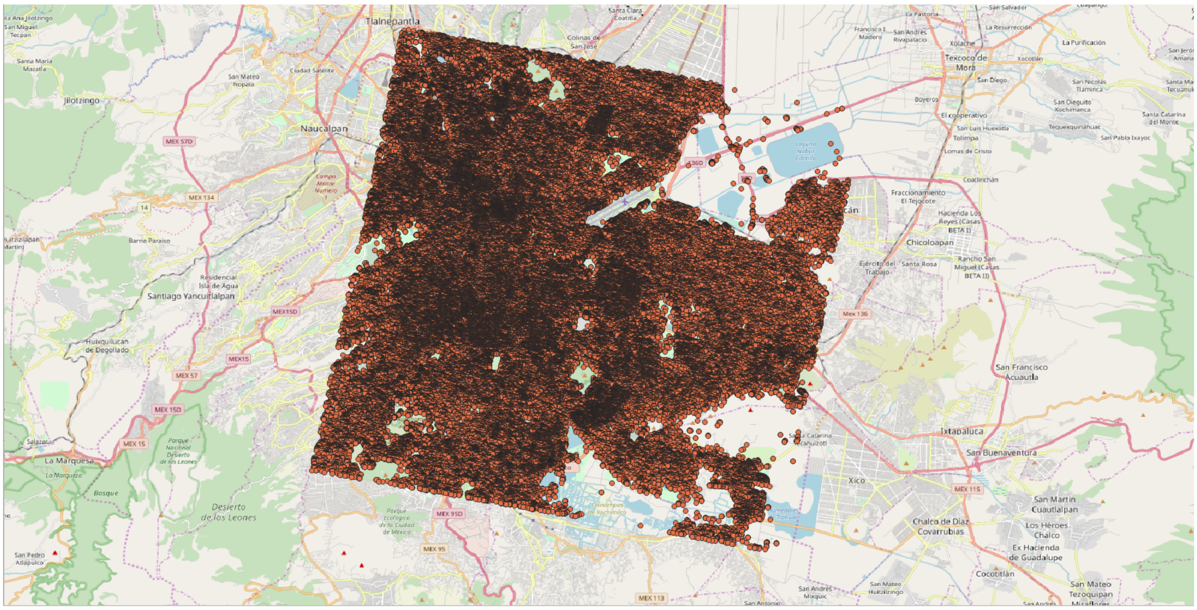

Figure 4.15: PSs found using amplitude dispersion of 0.25. The brown dots represent the PSs across the area of interest. Mexico City is very densely built which explains the closely spaced PSs. It clearly demarcates the parks and water bodies from the build infrastructure.

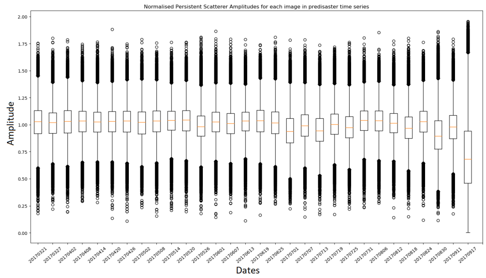

(a) Scaled PS amplitudes over the whole time series

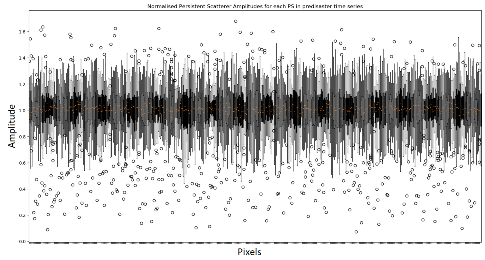

(b) Scaled Amplitudes of all images over subset of PSCs

Figure 4.16: The images show boxplots that describe the general trends of the scaled amplitudes of PS over the pre-disaster time period for Mexico City.

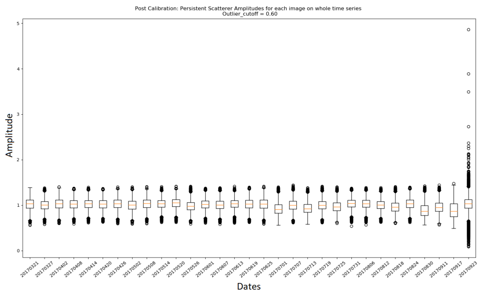

(a) PS amplitudes over the whole time series after outlier removal

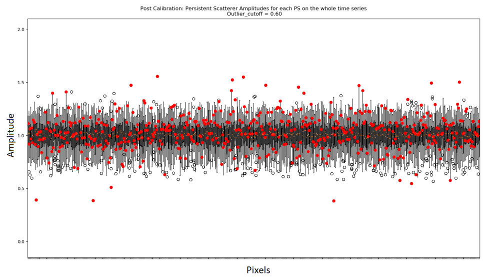

(b) Amplitudes of all images over subset of PSCs after outlier removal

Figure 4.17: The images show boxplots of PS amplitudes after outlier removal and describes how the post-disaster image shows marked variations from the pre-disaster timeline for Mexico City

the coherence of the image pairs immediately preceding the earthquake is also low compared to the average coherence of the rest of the pre-disaster image pairs. It could be due to some instrument error but this is speculation.

After the outliers are removed as explained in section 3.1.2, amplitude trends are as shown in Figures 4.17a and 4.17b. Most of the values are centred between 0.5 and 1.5. The largest variations are seen in the post-disaster image, as expected. The red points in Figure 4.17b represent the amplitude values of the post-disaster image. Most of these values are expected to be part of the outliers of the boxplot but we see that that is not the case. This could be due to a loss in amplitude signal caused by multiple bounces from small, densely built infrastructure [30].

Subsequently, the change detection method is applied to the final set of PSs as described in 3.1.3. The output is normalised between the values of 0 and 1, colour coded over a gradient ranging from yellow to red representing slight damage to highly damaged, and the points overlayed on Google Earth. This output is in the form of csv files so it can easily be imported into Google Earth or QGIS for viewing or analysis.

Unfortunately, there is no damaged grading map available from EMS. Therefore, a crowdsourced map is used [12], which is also used by the ARIA team from NASA JPL for producing a damage proxy map of the Mexico City earthquake. This is shown in Figure 4.18. The damage level is graded from yellow to red, ranging from low damage to highly damaged. The purple pointers represent areas with gas leaks and grey represents no data. We assume the damaged points here to be correct, though it is not thoroughly verified and investigated across the entire city.

The results of the methodology applied to the PSs are shown in Figure 4.19. The results are not a very good match. A lot of points are found towards the eastern part of the city that do not coincide with the crowdsourced details. It might be due to some other reasons such as construction but this is just speculation. The points found in the centre of the city are more accurate. Overall, 27 pixels were found to be damaged out of which around 7 matches with the reference map. This indicates a true positive rate of 25% for Mexico City.

The full-resolution images are then spatially averaged (or multilooked) by a factor of 4x12. This value is chosen because Mexico city is a large area which is very densely packed and we would not be losing much information with a bigger multilooking vector. The results of this method give slightly better results than that

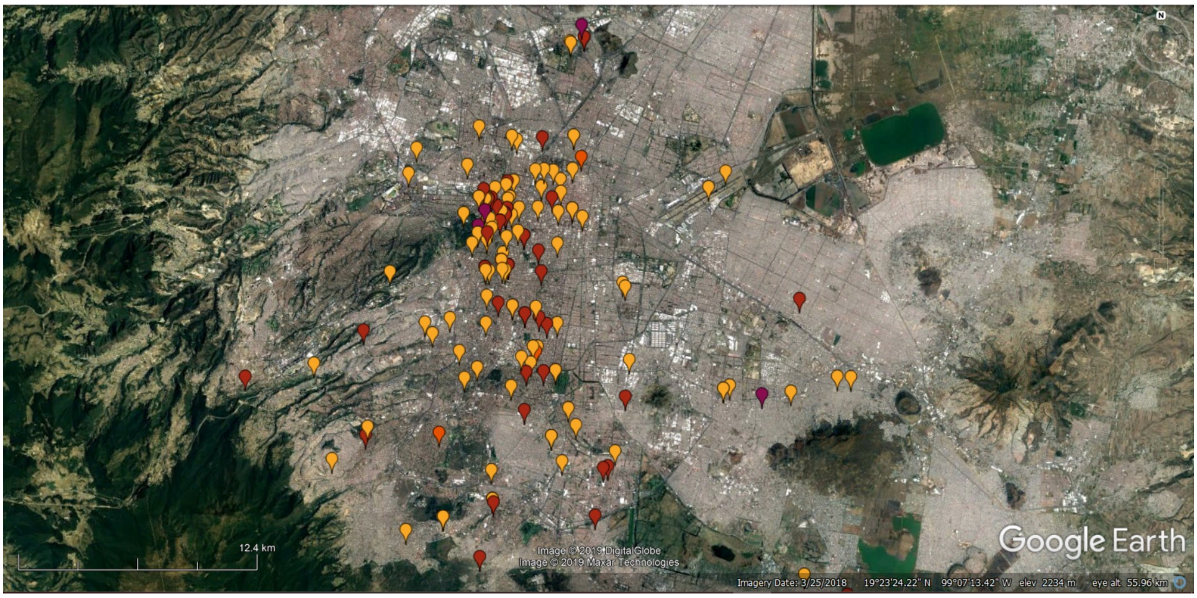

Figure 4.18: Crowd sourced map depicting collapsed and damaged Building after the M 7.1 19th September Puebla Earthquake. The damage level is graded from yellow to red, ranging from low damage to highly damaged. The purple pointers represent areas with gas leaks and grey represents no data. This map has not been verified in-situ.

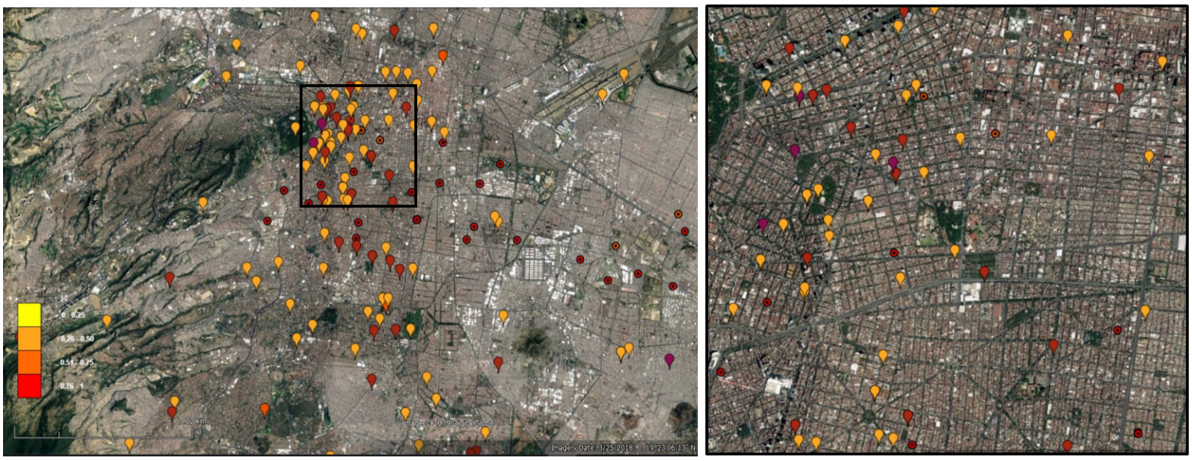

Figure 4.19: Results of the methodology applied to PS amplitudes derived from full-resolution images of Mexico City after the M7.1 2017 Puebla earthquake. To the left is the full-scale image showing the entire region under consideration. To the right, the magnified image of the most affected part of the city is pictured. The PSs do not provide an accurate representation of the damage sans a few areas.

Figure 4.20: Results of the methodology applied to multilooked (4x12) amplitudes of Mexico City after the M7.1 2017 Puebla earthquake. To the left is the full-scale results for the area under consideration and to the right is the zoomed-in image of the most damaged part of the city. This performs slightly better than the PSs but it does not identify a lot of the points characterised as damaged in the crowdsourced map.

of the PSs towards the mid-western part of the city where most of the damage is concentrated. However, there are a significant number of points that are unaccounted for mostly towards the eastern part of the city. Out of a total of 65 points detected as damaged, about 11 of them match with the reference map. This gives us a true positive rate of about 17%.

When the image is adaptively multilooked as explained in 3.2.2, with a multilooking vector of 4x12, the results derived are as shown in 4.21. This gives a very similar result to the boxcar averaging method. Overall, the amplitude values have not been reliable in terms of providing accurate results when compared to the available reference map.

Finally, the coherence values are investigated. Figure 4.22 shows the coherence of a pre-disaster pair and the co-disaster pair. There is a big degradation in the coherence of the image pairs after the occurrence of the earthquake. Figure 4.23 illustrates the output of the algorithm. Immediately, we see that the coherence parameter performs much better in terms of identifying damaged areas. In the mid-western part of the city, where most of the damaged points are indicated in the reference map, a cluster of points are correctly identified by the algorithm. A zoomed-in image of this are is shown in Figure 4.24. Out of the 125 points classified as damaged, around 45 of them are correct according to the reference map used. This results in a true positive rate of 36%.

While collectively looking at all of the results from each parameter, it is obvious that the coherence has performed much better than the other two. Among the correctly categorised points, none of the methods provides repeat values, that is, all the correctly classified points are unique. Although there are a few points (around 5) scattered across the city which do not match with the crowdsourced reference map that repeatedly shows up as damaged using multiple methods. One can speculate about the nature of the changes but there is currently no other way to verify it. For Mexico City, the total number of true positives stands at around 30%, with the coherence giving more accurate results.

Table 4.4: Table showing the accuracy of the results of the methodology used for Mexico City, which includes the number of points detected as damaged and the percentage of those correctly determined to be damaged (True Positives) for parameters used, individually and combined

	PS	Amplitude	Coherence	Overall
No. of points detected	27	65	125	217
True Positives	25.9%	16.92%	36.0%	29.03%

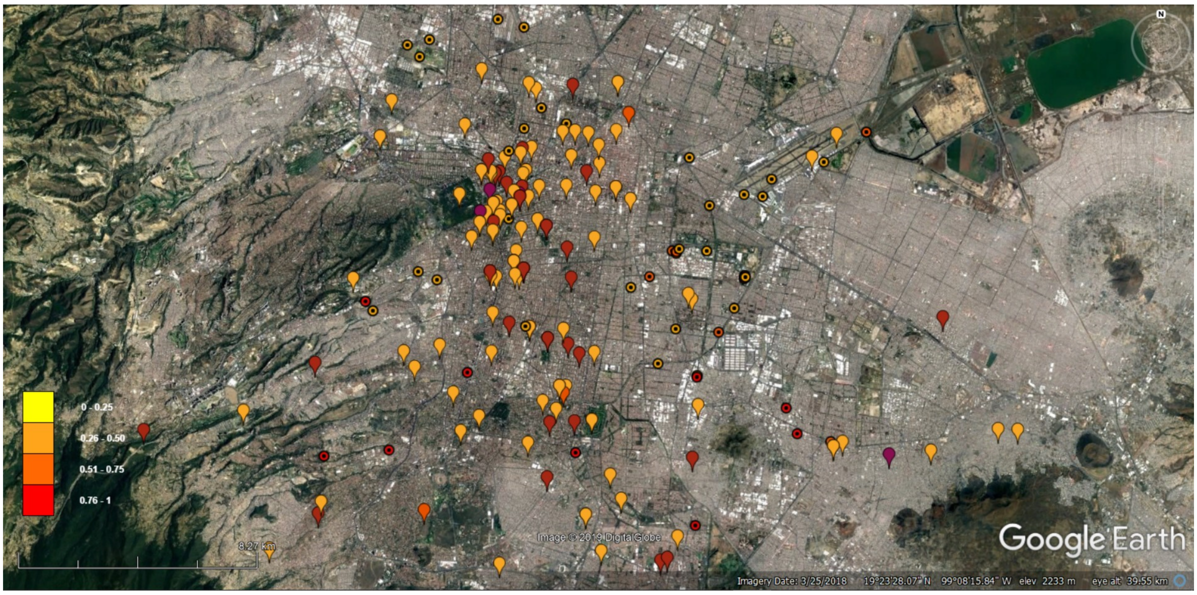

Figure 4.21: Results of the methodology applied to adaptively multilooked (4x12) amplitudes of Mexico City after the M7.1 2017 Puebla earthquake. The results are largely similar to the results of boxcar multilooking.

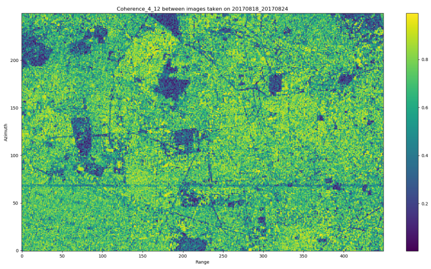

(a) Coherence of Mexico City area between image pairs 18 August 2017 and 24 August 2017

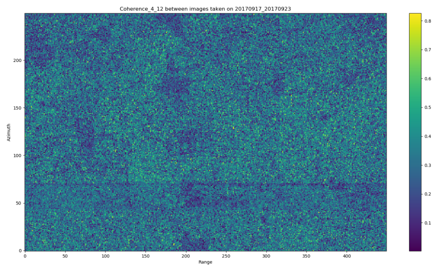

(b) Coherence of Mexico City area between image pairs 17 September 2017 and 23 September 2017

Figure 4.22: The images represent the change in coherence over the time-series. The image to the left show the pre-disaster coherence which is high and the image on the right show the co-disaster or co-seismic coherence which is very low implying there was a temporal decorrelation.

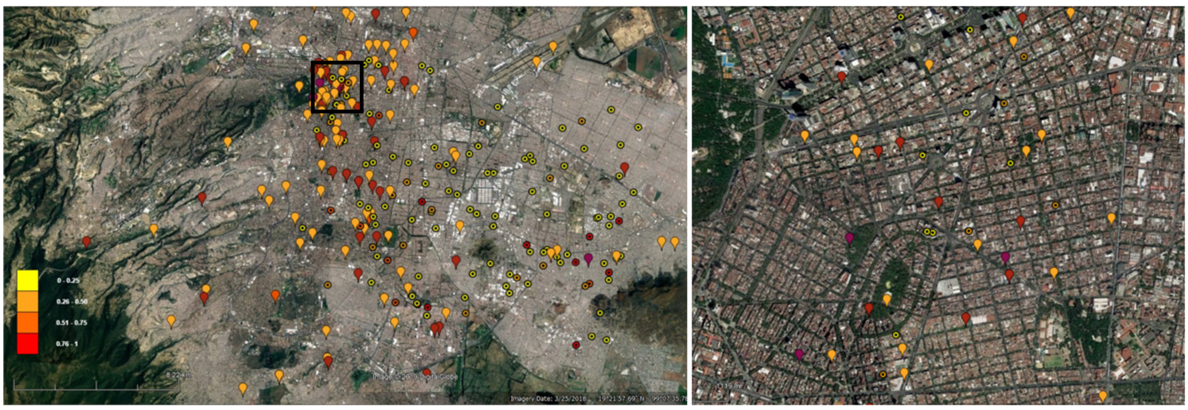

Figure 4.23: Results of the methodology applied to coherence values from multilooked (4x12) images of Mexico City after the M7.1 2017 Puebla earthquake. A full-scale image of the entire area under consideration is depicted to the left. On the right, a magnified image of the part of the city which was most affected is shown. While not all damaged buildings are identified, a lot of clusters of damaged buildings are identified. Coherence performs the best compared to the other two amplitude dependent parameters.

Figure 4.24: Results of the methodology from all parameters applied to Mexico City after the M7.1 2017 Puebla earthquake. The image below shows the results from all the parameters together in one collective map. To see the contribution of each parameter to this map, the three call-outs are pictured. To the top left, we see the results from the PSs. In the middle, the multilooked amplitude results are shown and to the top right, the coherence results are portrayed. The coherence parameter works the best in comparison to the rest fo the two parameters with a collective true positive rate of 30%.

5

Discussion and Conclusion

In this chapter, a discussion of the main results is presented according to the thesis objectives formulated at the beginning of the research. The sub-questions being:

SQ1 *How can the Sentinel 1 archive be used effectively for detecting building damage?*

The Sentinel mission makes radar images available freely with its open access policy. The large scale open and free access policy maximises the beneficial utilisation of the dataset for a wide range of applications including building damage detection. The Level 1 products are made available within 24 hours of observation. The satellite has a short temporal resolution, with a repeat cycle of 6-12 days which makes it very suitable for using the images in a time-series analysis.

Each image acquired has a spatial resolution of 5 m by 20 m so the research benefits from the medium resolution data. These are in the form of Single Look Complex (SLC) images which consist of both amplitude and phase information.

The time-series is analysed by considering the three main parameters - PSs, multilooked amplitude and multilooked coherence. This is applied to the areas of Amatrice in Italy and Mexico City in Mexico, both of which sustained devastating earthquakes. A time-series of 31 images is used in consideration of 1) information that can be learnt from using a long time series, 2) time required to download and process the data and 3) selecting a reliable number of PS candidates. Most of the organisations that produce damage maps for emergencies still use bi- or tri- temporal analysis, possibly due to time constraints or unavailability of Sentinel data at the time. The time-series analysis performed in this research takes less than 8 hours, most of which is downloading and pre-processing time. The time taken to execute the processes after RIPPL's pre-processing takes an hour.

The primary limitation of this is the time taken to download and preprocess the data but one can speculate, knowing how fast technology has improved over the years, processing power will only increase in future. The results of the methodology have also been largely very accurate for the region of Amatrice as shown in Chapter 4.

Therefore the Sentinel 1 archive is used to perform time-series analysis and the results of it are described in Chapter 4.

SQ2 *How can the use of amplitude and coherence parameters be combined to produce damage maps?*

The amplitude and the phase parameters can be used complementary to each other since the two parameters are sensitive to different backscattering. In their paper, Matsuoka and Yamazaki [33] found that while the amplitude can find large surface changes, the coherence is sensitive to small changes. Hence, a similar approach is followed for this research where complex SLCs are used to identify changes in amplitude and phase.

In addition to using multilooked amplitude and phase as in [33, 44], PSs, derived from full resolution (unmultilooked) images are also used. PSs are points that are stable in amplitude over a long period of time. These also act as an incredible proxy to built structures and actively 'mask' vegetation and water bodies as shown in Figures 4.15 and 4.3.

From the two case studies, we also see a difference in the functionality of the parameter and what it senses. In Amatrice, a hilltop town which was devastated in the earthquake sustained massive building damage. Over half the buildings were destroyed including almost the entire historic town, despite many buildings being reinforced since they were built in the 16th, 17th and 18th centuries. In total, 293 historic buildings were damaged or destroyed [27]. This heavy damage was captured very well by the amplitude parameters, as expected, as well by coherence.

Although Mexico was struck by a larger earthquake, the most common building material used is reinforced concrete (Murakami [1996] [35]). Using this material generally increases the survival rate up to a time period of 6 days. The buildings that did collapse were primarily unreinforced concrete and brick masonry. The devastation was spread throughout Mexico's capital wherein 38 buildings completely collapsed and more than 5000 other building suffered varying levels of damage [41]. From the damage maps of Mexico City, the most accurate of the three parameters is coherence, which is known for identifying small changes. It is possible that due to the complex scattering mechanism of the closely built structures, the amplitude backscatter was not very useful in detecting changes but this speculation. In situations where the three maps are not complementary, it might be more useful to use the results of the coherence map since it identifies small changes and is not affected by the multiple bounce phenomenon like the amplitudes.

SQ3 *Can full resolution Sentinel 1 images be utilised effectively along with spatially averaged images?*

Spatially averaged or multilooked images are commonly used in order to reduce the effect of speckle-noise at the cost of spatial resolution. The multilooked images are then analysed in terms of amplitude and coherence to find changed points. In addition, full-resolution images are used for the possibility of detecting individual building damage using PSs.

In Amatrice, each parameter produced unique, non-overlapping points, except for once instance. The overlapping output helps validate the results further since it is verified by two separate signals. In the case of the non-overlapping results, it clearly shows the advantages of using full-resolution and multilooked images by detecting new and unique points.

In the case of Mexico, among the correctly categorised points, none of the methods provides repeat or overlapping results, that is, all the correctly classified points are unique. This again goes to show that there is value in using different levels of multilooking for images. However, there are a few points scattered across the city which do not match with the crowdsourced reference map that shows up as damaged using multiple methods. One can speculate about the nature of the changes but there is currently no other source to verify it.

Therefore, using different resolutions of images has its advantages in terms of identifying new, unique points which are correctly classified as damaged and in terms of validating points that are determined as damaged using multiple parameters.

SQ4 *Are the resulting damage maps sufficiently informative?*

Care has been taken to represent the maps in the most straightforward way possible. The damaged values are normalised within the range 0 to 1 for each of the parameters for uniformity. The outputs are initially generated in .csv files which can be imported into QGIS for further analysis or to Google Earth directly. It consists of the damage level, the latitude and longitude of the changed point.

The accuracy of the results varies for the two areas - Amatrice and Mexico City, considered for testing the algorithm. In the case of Amatrice, all the parameters performed equally well with a total true positives of 83% after vegetation masking. For Mexico City, this value stands at around 30%, with the coherence giving the most accurate results. Here true positives refer to points that are damaged and are identified as damaged by the algorithm.

In the business of damage detection, it is important to avoid true negatives, which is points that are actually damaged but are not detected by the algorithm. Ideally, this rate should be low. While the damage detection is not at a building level, there is definitely a good detection rate at a cluster level.

While the methodology described can be processed quickly, the data latency on ESAs part in terms of revisit time is the biggest limitation. Apart from this, it takes around 5.5 hours for ESA to process the raw data and make the Level 1 SLC format available. The downloading and preprocessing step takes another 6-7 hours. The software used, RIPPL, is still under development but once it is released, is an entirely pythonic implementation which allows easy manipulation of data and would be accessible by everyone.

Throughout this work, the focus was on developing an efficient methodology to help with locating damaged structures in case of a disaster. It is meant to help rapid response teams assess the situation and can be used for further planning according to the severity of the damage as shown in the maps. The methodology proposed does a good job of detecting damaged clusters of buildings.

More specifically, each of the methods helps in identifying different levels of damage. We learn through this research that there is certainly an added value in using PSs in the way that it has been - stable natural reflectors which can be used for large scale damage detection. We also learn that the results are improved by using full resolution images along with multilooked images. Therefore, combining the three parameters - PS, multilooked amplitude and multilooked coherence improves the overall efficiency of damage maps.

Overall, the Sentinel 1 imagery can be used to detect damage in case of rapid response situations.

5.1. Recommendations for Future Work

One of the things that will help in faster response times is by automating the whole process. Specifically, in this research, the amplitude dispersion threshold is still decided manually but it can be estimated based on the built density of a location. The final threshold, which decides if a point is damaged or not, is always greater than 1, but its exact value is also decided manually. It could be useful to devise an automatic method that decides these thresholds.

It could also be very useful to trigger the damage detection algorithm immediately once an earthquake is sensed by a region's seismic networks and if it is above a certain magnitude, as soon as the post-disaster image is available.

The algorithm, in theory, should be applicable to any situation which involves building damage such as situations of air strikes, building damage due to floods, cyclones etc. This has to be tested and validated further.

According to Voigt [48], in the aftermath of the 2019 Haiti earthquake, the global coordination of the satellite mapping response turned out to be chaotic and challenging. While there is a multitude of damage maps being produced and researched, it would be more efficient to hand over the algorithmic process to a centralised body that can distribute the maps operationally to search and rescue forces that can easily access them using an open data policy.

Another approach that can be considered is to improve the revisit time of the concerned satellite to less than the current 6-12 days in case of the Sentinel mission. But perhaps the most effective thing to do would be for earthquake-prone regions to adopt earthquake-resistant building practises. In Japan, building regulations were set in 1981, wherein all new structures have to comply with earthquake-proof standards set by law. This standard focuses not only on preventing the collapse of buildings during earthquakes but also on how to secure the safety of the people inside them. More regulations and amendments were introduced later to make the building even more strong.

Bibliography

[1] Agency Reform. Ssa 51 reports serious injuries. https://www.elindependientedehidalgo.com.mx/reporta-ssa-51-lesionados-graves/.

[2] American Red Cross. How Long Can a Person Survive Under Earthquake Debris? https://www.issuelab.org/resources/21683/21683.pdf.

[3] Gustavo A Arciniegas, Wietske Bijker, Norman Kerle, and Valentyn A Tolpekin. Coherence-and amplitude-based analysis of seismogenic damage in bam, iran, using envisat asar data. *IEEE Transactions on Geoscience and Remote Sensing*, 45(6):1571–1581, 2007.

[4] Matus Bakon, Daniele Perissin, Milan Lazecky, and Juraj Papco. Infrastructure non-linear deformation monitoring via satellite radar interferometry. *Procedia Technology*, 16:294–300, 2014.

[5] Stefan V Baumgartner and Gerhard Krieger. Multi-channel sar for ground moving target indication. In *Academic Press Library in Signal Processing*, volume 2, pages 911–986. Elsevier, 2014.

[6] Paolo Berardino, Gianfranco Fornaro, Riccardo Lanari, and Eugenio Sansosti. A new algorithm for surface deformation monitoring based on small baseline differential sar interferograms. *IEEE transactions on geoscience and remote sensing*, 40(11):2375–2383, 2002.

[7] Roland Bürgmann, Paul A Rosen, and Eric J Fielding. Synthetic aperture radar interferometry to measure earth's surface topography and its deformation. *Annual review of earth and planetary sciences*, 28(1): 169–209, 2000.

[8] S Chelbi, A Khireddine, and JP Charles. Interferometry process for satellite images sar. In *2011 7th International Conference on Electrical and Electronics Engineering (ELECO)*, pages II–200. IEEE, 2011.

[9] Christopher Sherman from AP News. They recover body of last victim of the earthquake in Mexico. https://earthquake.usgs.gov/earthquakes/eventpage/us2000ar20/executive.

[10] Andrew W Coburn, Robin JS Spence, and Antonios Pomonis. Factors determining human casualty levels in earthquakes: mortality prediction in building collapse. In *Proceedings of the First International Forum on Earthquake related Casualties. Madrid, Spain, July 1992*, 1992.

[11] Copernicus Emergency Management Service. [EMSR177] Amatrice Aerial: Grading Map. https://emergency.copernicus.eu/mapping/ems-product-component/EMSR177_20AMATRICEAERIAL_GRADING_OVERVIEW/3.

[12] Crowd-Sourced. Map of Buildings Collapsed and Damaged by the Earthquake of 09/19/2017. https://www.google.com/maps/d/u/0/viewer?mid=1_-V97lbdgLFHpx-CtqhLWlJAnYY&ll=19.37635697365096%2C-99.10908134721183&z=12.

[13] C. Deledalle, L. Denis, and F. Tupin. Nl-insar: Nonlocal interferogram estimation. *IEEE Transactions on Geoscience and Remote Sensing*, 49(4):1441–1452, April 2011. ISSN 0196-2892. doi: 10.1109/TGRS.2010.2076376.

[14] EMDAT (2019): OFDA/CRED International Disaster Database, Université catholique de Louvain – Brussels – Belgium. Number of reported natural disasters. . https://ourworldindata.org/natural-disasters#number-of-reported-disaster-events.

[15] ESA. "Sentinel 1 Level 1 Algorithm Definition", . https://sentinel.esa.int/documents/247904/1877131/Sentinel-1-Level-1-Detailed-Algorithm-Definition.

[16] ESA. "Sentinel 1 Product Specification", .

[17] ESA. "Level 1 Radiometric Calibration", . https://sentinel.esa.int/web/sentinel/radiometric-calibration-of-level-1-products.

[18] Alessandro Ferretti, Claudio Prati, and Fabio Rocca. Permanent scatterers in sar interferometry. *IEEE Transactions on geoscience and remote sensing*, 39(1):8–20, 2001.

[19] Alessandro Ferretti, Alfio Fumagalli, Fabrizio Novali, Claudio Prati, Fabio Rocca, and Alessio Rucci. A new algorithm for processing interferometric data-stacks: Squeesar. *IEEE Transactions on Geoscience and Remote Sensing*, 49(9):3460–3470, 2011.

[20] Eric J Fielding, Morteza Talebian, Paul A Rosen, Hamid Nazari, James A Jackson, Manoucher Ghorashi, and Richard Walker. Surface ruptures and building damage of the 2003 bam, iran, earthquake mapped by satellite synthetic aperture radar interferometric correlation. *Journal of Geophysical Research: Solid Earth*, 110(B3), 2005.

[21] Paolo Gamba, Fabio Dell'Acqua, and Giovanna Trianni. Rapid damage detection in the bam area using multitemporal sar and exploiting ancillary data. *IEEE Transactions on Geoscience and Remote Sensing*, 45(6):1582–1589, 2007.

[22] Fabio Gatelli, A Monti Guamieri, Francesco Parizzi, Paolo Pasquali, Claudio Prati, and Fabio Rocca. The wavenumber shift in sar interferometry. *IEEE Transactions on Geoscience and Remote Sensing*, 32(4): 855–865, 1994.

[23] Hans Driessen. "Lecture 2 - Radar Systems Notes", 2018. https://brightspace.tudelft.nl/d2l/le/content/126478/Home.

[24] Ramon F Hanssen. *Radar interferometry: data interpretation and error analysis*, volume 2. Springer Science & Business Media, 2001.

[25] E Weber Hoen and Howard A Zebker. Penetration depths inferred from interferometric volume decorrelation observed over the greenland ice sheet. *IEEE Transactions on Geoscience and Remote Sensing*, 38 (6):2571–2583, 2000.

[26] J Hoffmann. Mapping damage during the bam (iran) earthquake using interferometric coherence. *International Journal of Remote Sensing*, 28(6):1199–1216, 2007.

[27] ICCROM - International Centre for the Study of the Preservation and Restoration of Cultural Property. "Italy Earthquake's Other Casualty – Cultural Heritage". https://www.iccrom.org/news/italy-earthquakes-other-casualty-cultural-heritage.

[28] International Federation of Red Cross and Red Crescent Societies. "What is a disaster?". https://www.ifrc.org/en/what-we-do/disaster-management/about-disasters/what-is-a-disaster/.

[29] Joseph Castro. How Long Can a Person Survive Under Earthquake Debris? https://www.livescience.com/16747-earthquake-rubble-survival.html.

[30] Kalev Koppel, K Zalite, Kaupo Voormansik, and Thomas Jagdhuber. Sensitivity of sentinel-1 backscatter to characteristics of buildings. *International Journal of Remote Sensing*, 38(22):6298–6318, 2017.

[31] Fuk K Li and Richard M Goldstein. Studies of multibaseline spaceborne interferometric synthetic aperture radars. *IEEE Transactions on Geoscience and Remote Sensing*, 28(1):88–97, 1990.

[32] Masashi Matsuoka and Fumio Yamazaki. Interferometric characterization of areas damaged by the 1995 kobe earthquake using satellite sar images. In *Proceedings of the 12th World Conference on Earthquake Engineering*, volume 2, 2000.

[33] Masashi Matsuoka and Fumio Yamazaki. Use of interferometric satellite sar for earthquake damage detection. *Sat*, 2:z1, 2000.

[34] Masashi Matsuoka and Fumio Yamazaki. Use of satellite sar intensity imagery for detecting building areas damaged due to earthquakes. *Earthquake Spectra*, 20(3):975–994, 2004.

[35] Hitomi Murakami. Chances of occupant survival and sar operation in the buildings collapsed by the 1995 great hanshin earthquake, japan. In *Proc. 11th World Conf. on Earthq. Engr., Paper*, number 852, 1996.

[36] Edwin Nissen, Tadashi Maruyama, J Ramon Arrowsmith, John R Elliott, Aravindhan K Krishnan, Michael E Oskin, and Srikanth Saripalli. Coseismic fault zone deformation revealed with differential lidar: Examples from japanese mw 7 intraplate earthquakes. *Earth and Planetary Science Letters*, 405: 244–256, 2014.

[37] A. Parizzi and R. Brcic. Adaptive insar stack multilooking exploiting amplitude statistics: A comparison between different techniques and practical results. *IEEE Geoscience and Remote Sensing Letters*, 8(3): 441–445, May 2011. ISSN 1545-598X. doi: 10.1109/LGRS.2010.2083631.

[38] Gilles Peltzer and Paul Rosen. Surface displacement of the 17 may 1993 eureka valley, california, earthquake observed by sar interferometry. *Science*, 268(5215):1333–1336, 1995.

[39] R. K. Raney. Radar fundamentals: Technical perspective. *Principals and Applications of Imaging Radar, Manual of Remote Sensing*, 1998.

[40] Jonathan Reades, Francesco Calabrese, Andres Sevtsuk, and Carlo Ratti. Cellular census: Explorations in urban data collection. *IEEE Pervasive computing*, 6(3):30–38, 2007.

[41] Eduardo Reinoso, Miguel A Jaimes, and Marco A Torres. Evaluation of building code compliance in mexico city: mid-rise dwellings. *Building Research & Information*, 44(2):202–213, 2016.

[42] Paul A Rosen, Scott Hensley, Ian R Joughin, Fuk K Li, Soren N Madsen, Ernesto Rodriguez, and Richard M Goldstein. Synthetic aperture radar interferometry. *Proceedings of the IEEE*, 88(3):333–382, 2000.

[43] S Stramondo, M Moro, C Tolomei, FR Cinti, and F Doumaz. Insar surface displacement field and fault modelling for the 2003 bam earthquake (southeastern iran). *Journal of Geodynamics*, 40(2-3):347–353, 2005.

[44] S Stramondo, C Bignami, M Chini, N Pierdicca, and A Tertulliani. Satellite radar and optical remote sensing for earthquake damage detection: results from different case studies. *International Journal of Remote Sensing*, 27(20):4433–4447, 2006.

[45] Giovanna Trianni and Paolo Gamba. Fast damage mapping in case of earthquakes using multitemporal sar data. *Journal of Real-Time Image Processing*, 4(3):195–203, 2009.

[46] USGS. M 7.1 - 1km E of Ayutla, Mexico. `https://earthquake.usgs.gov/earthquakes/eventpage/us2000ar20/executive`.

[47] Jeroen van Heyningen. Rapid building damage detection through sar timeseries analysis in the google earth engine: Using sentinel-1 grd imagery in the google earth engine to detect building damage in rapid disaster response situations. 2018.

[48] Stefan Voigt, Tobias Schneiderhan, André Twele, Monika Gähler, Enrico Stein, and Harald Mehl. Rapid damage assessment and situation mapping: learning from the 2010 haiti earthquake. *Photogrammetric Engineering and Remote Sensing*, 77(9):923–931, 2011.

[49] Tuong Thuy Vu, Masashi Matsuoka, and Fumio Yamazaki. Lidar signatures to update japanese building inventory database. In *25th Asian Conference on Remote Sensing*, 2004.

[50] Tuong Thuy Vu, Masashi Matsuoka, and Fumio Yamazaki. Lidar-based change detection of buildings in dense urban areas. In *IGARSS 2004. 2004 IEEE International Geoscience and Remote Sensing Symposium*, volume 5, pages 3413–3416. IEEE, 2004.

[51] Wallemacq, Pascaline and House, Rowena. Economic losses, poverty and disasters: 1998-2017. `https://www.preventionweb.net/publications/view/61119`.

[52] WHO. Natural Events. `https://www.who.int/environmental_health_emergencies/natural_events/en/`.

[53] Sang-Ho Yun, Kenneth Hudnut, Susan Owen, Frank Webb, Mark Simons, Patrizia Sacco, Eric Gurrola, Gerald Manipon, Cunren Liang, Eric Fielding, et al. Rapid damage mapping for the 2015 m w 7.8 gorkha earthquake using synthetic aperture radar data from cosmo–skymed and alos-2 satellites. *Seismological Research Letters*, 86(6):1549–1556, 2015.

A

Damage Detection Maps

A.1. Case Study 1: Amatrice, M6.2 2016 Central Italy Earthquake

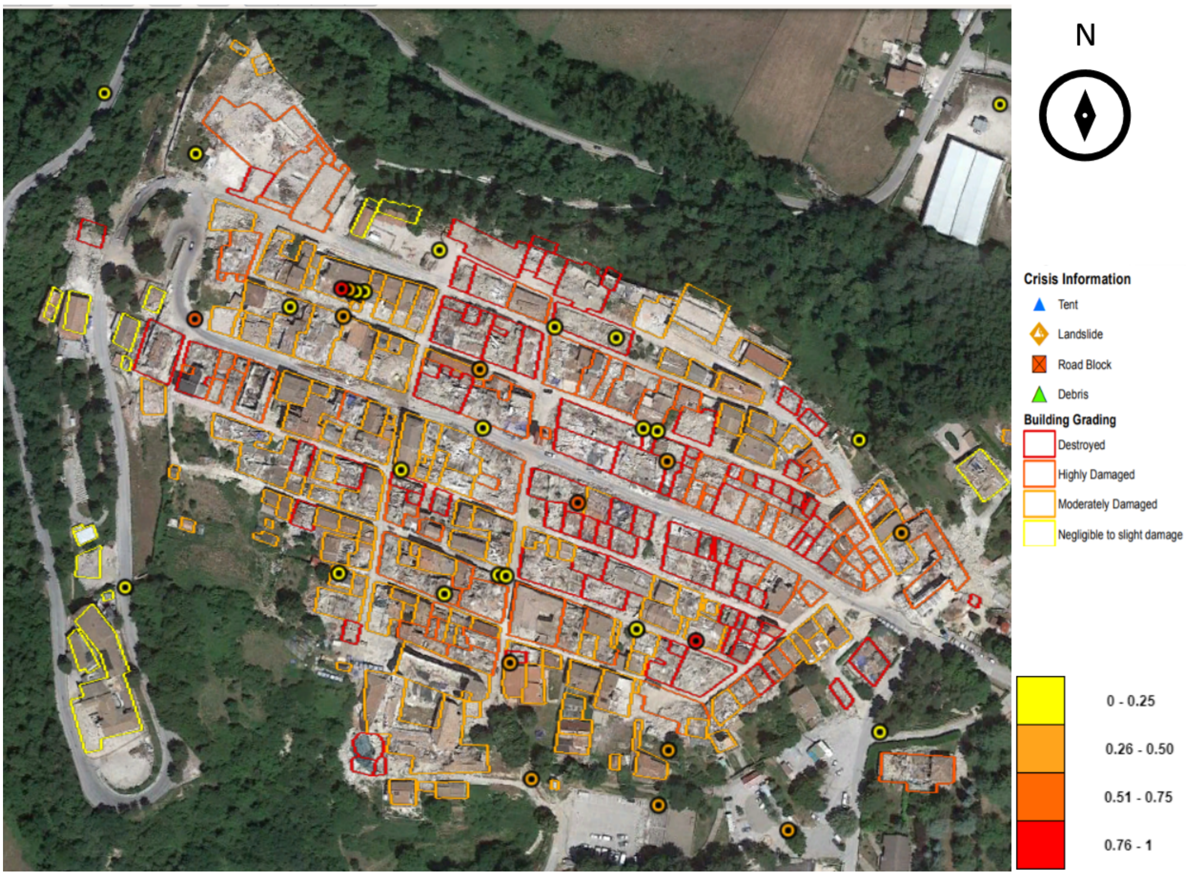

Figure A.1: Enlarged results of the methodology applied to all the parameters during the M6.2 Central Italy earthquake in 2016. The damaged points derived from the methodology are indicated by coloured circles ranging from red to yellow representing heavily damaged to slightly damaged areas. The image represents the north-western part of Amatrice where most of the historical buildings were situated. This require suffered the most infrastructural damage in the town.

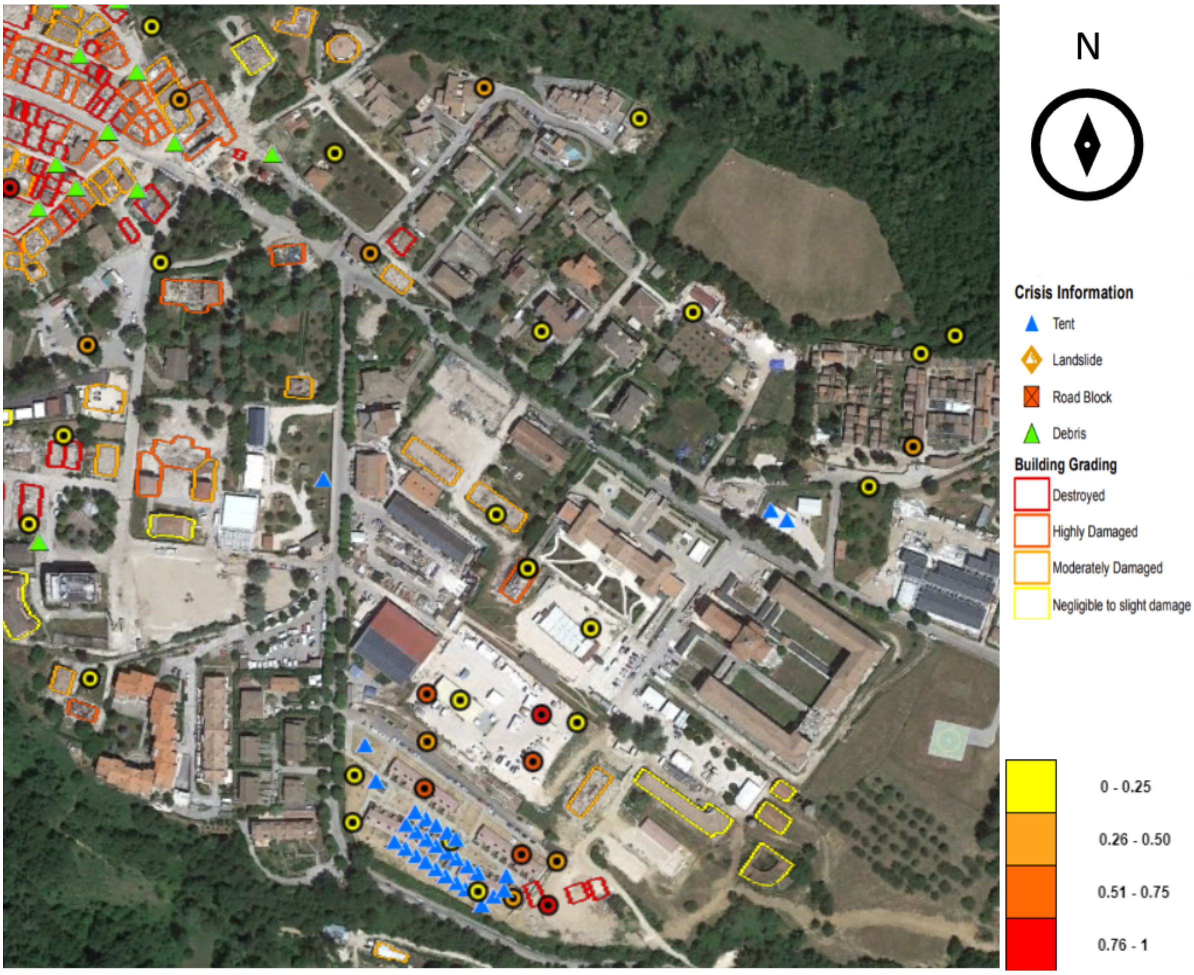

Figure A.2: Enlarged results of the methodology applied to all the parameters during the M6.2 Central Italy earthquake in 2016. The damaged points derived from the methodology are indicated by coloured circles ranging from red to yellow representing heavily damaged to slightly damaged areas. The image shows the central part of Amatrice where some relief camps were set up soon after the disaster, which is indicated by the blue cones (from Grading map) and this is captured by the pixel amplitude and coherence parameters. A few outliers are also seen.

Figure A.3: Enlarged results of the methodology applied to all the parameters during the M6.2 Central Italy earthquake in 2016. The damaged points derived from the methodology are indicated by coloured circles ranging from red to yellow representing heavily damaged to slightly damaged areas. This image shows the south-eastern part fo Amatrice where some relief camps were set up as represented by the blue cones to the left. A cluster of points is seen the right which turns out to be an area that was used as a parking lot soon after the disaster. This is shown separately in the following image.

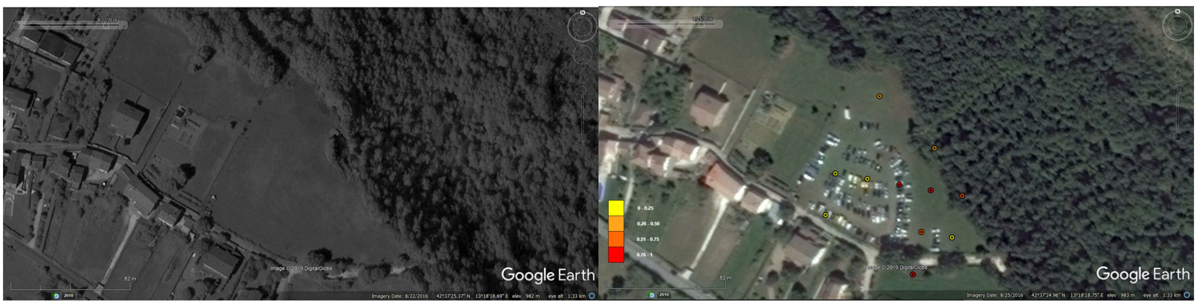

(a) Eastern part of Amatrice before the earthquake on 22 August 2016

(b) Eastern part of Amatrice after the earthquake on 25 August 2016

Figure A.4: Eastern end of Amatrice which was used as a car parking area after the earthquake as observed from Google Earth historical images. This change is also picked up by the methodology used with boxcar multilooked (2x6) images and coherence.

A.2. Case Study 2: Mexico City, M7.8 2017 Puebla Earthquake

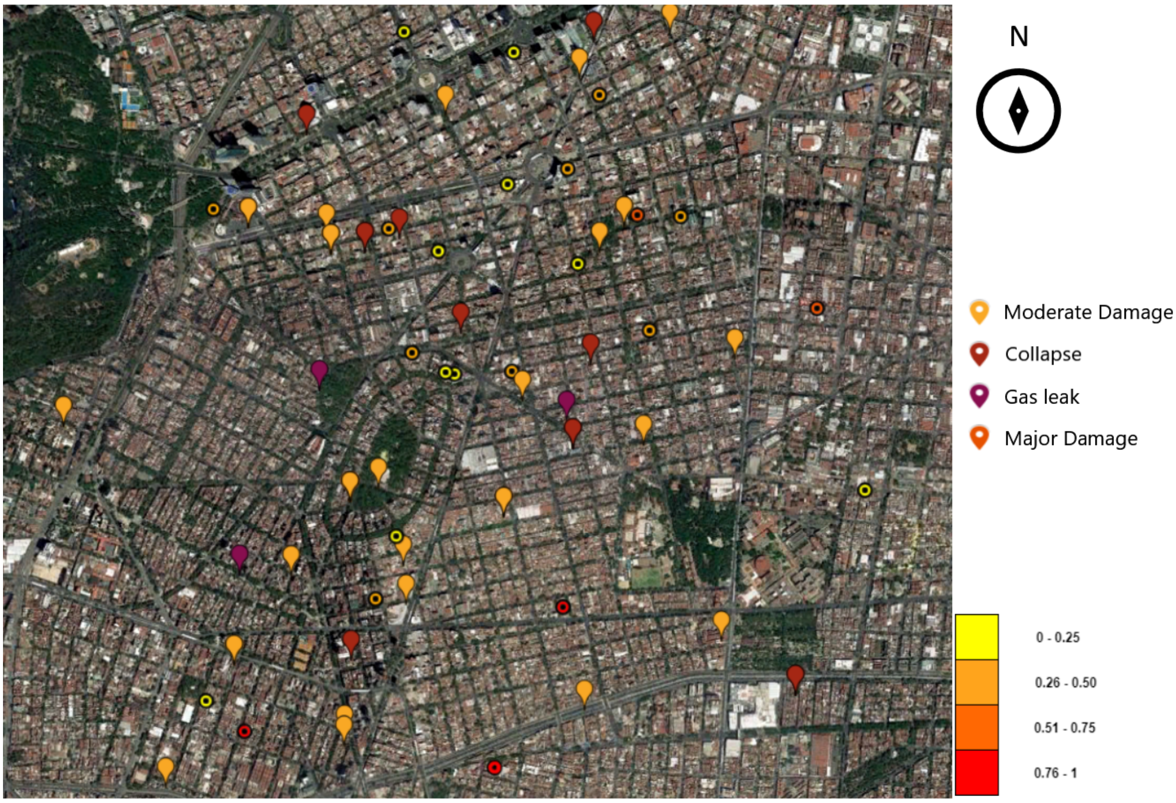

Figure A.5: Enlarged results of the methodology applied to Mexico City during the M6.2 Central Italy earthquake in 2016. The damaged points derived from the methodology are indicated by coloured circles ranging from red to yellow representing heavily damaged to slightly damaged areas. The images shows the most heavily damaged part of the city.